

**POST PROCESSING METHODS FOR THREE DIMENSIONAL
IMAGING LIDAR WITH MULTI-SCALE CHARACTERIZATION OF
SUBSEA ORGANISMS**

by

Trevor Lee McKenzie

A Thesis Submitted to the Faculty of
The College of Engineering and Computer Science
in Partial Fulfillment of the Requirements for the Degree of
Master of Science

Florida Atlantic University

Boca Raton, FL

December 2019

Copyright 2019 by Trevor Lee McKenzie

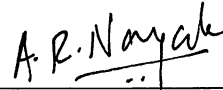
**POST PROCESSING METHODS FOR THREE DIMENSIONAL
IMAGING LIDAR WITH MULTI-SCALE CHARACTERIZATION OF
SUBSEA ORGANISMS**

by

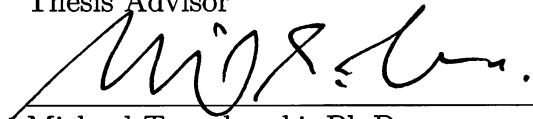
Trevor Lee McKenzie

This thesis was prepared under the direction of the candidate's thesis advisor, Dr. Aditya Nayak, Department of Ocean and Mechanical Engineering, and has been approved by the members of his supervisory committee. It was submitted to the faculty of the College of Engineering and Computer Science and was accepted in partial fulfillment of the requirements for the degree of Master of Science.

SUPERVISORY COMMITTEE:



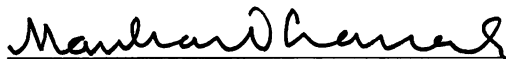
Aditya Nayak, Ph.D.
Thesis Advisor



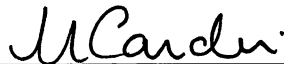
Michael Twardowski, Ph.D.



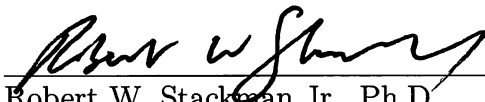
Fraser Dalgleish, Ph.D.



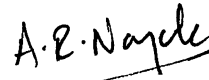
Manhar Dhanak, Ph.D.
Chair, Department of Ocean and Mechanical Engineering



Stella Batalama, Ph.D.
Dean, The College of Engineering and Computer Science



Robert W. Stackman Jr., Ph.D.
Dean, Graduate College



Aditya Nayak, Ph.D.

4-23-19

Date

ACKNOWLEDGEMENTS

Harbor Branch Oceanographic Institute

NOAA Cooperative Institute for Ocean Exploration, Research and Technology

Micheal Twardowski, Aditya Nayak, Fraser Dalglish

ABSTRACT

Author: Trevor Lee McKenzie
Title: Post Processing methods for three dimensional imaging lidar with multi-scale characterization of subsea organisms
Institution: Florida Atlantic University
Thesis Advisor: Dr. Aditya Nayak
Degree: Master of Science
Year: 2019

The thesis objective is to develop protocols that provide analysis and interpretation for data from a pulsed laser serial scanning lidar system for underwater imaging. The specific focus is remotely observing marine organisms in the centimeter size range in the poorly understood mesopelagic realm of the ocean. The Unobtrusive Multi-Static Lidar Imager (UMSLI) system captures an expansive volume scan field with differentiating imaging resolution per planar slice, allowing precise assignment of location for organisms in the field of view. The multi-static highly collimated beams are recorded by a photo-multiplier tube receiver as a time lapse waveform of the returned energy flux, each waveform comprehensibly represents an image pixel in spatially and temporally. Compiled lidar waveforms produce an array of returns which signify the magnitude of backscatter from varying sized particles across the observed volume. These volume scans are uniquely evaluated and transformed for each time bin through a processing method which extracts particle characteristics and statistics based on adaptive spatial and temporal techniques. The post processing method aims to greatly extend the capabilities of the lidar imaging system to extract particles. Results of the processing method are presented as particle counts

and particle size distributions of the water columns during observed vertical migration periods. Methods are compared with other optical devices for validation, and results are interpreted to better understand the organism distribution in the mesopelagic and their behavior, with respect to diel vertical migrations.

**POST PROCESSING METHODS FOR THREE DIMENSIONAL
IMAGING LIDAR WITH MULTI-SCALE CHARACTERIZATION OF
SUBSEA ORGANISMS**

List of Tables	ix
List of Figures	x
1 Introduction	1
1.1 Basics of underwater lidar	4
1.2 Underwater Lidar imaging	10
1.3 Development of UMSLI	13
2 UMSLI System and Experiment setup	17
2.1 UMSLI construction	17
2.2 Deployment setup	21
3 Data Acquisition	24
3.1 System and data configuration	24
3.2 Noise characteristics	26
4 Processing Methods	30
4.1 Resampling	33
4.2 Background subtraction	34
4.3 Thresholding	37
4.4 Masking	40
4.5 Extraction and resizing of POI	42

5	Results and Discussion	45
5.1	Water column profile	46
5.2	Particle concentrations	47
5.3	Particle Size Distributions	50
6	Conclusion	56
	Bibliography	59

LIST OF TABLES

4.1	Table of POI characteristics from figure 4.11	43
-----	---	----

LIST OF FIGURES

1.1	Time-series response of lidar signal: red waveforms represents multi-scatter case with small target return, blue waveform represent ideal case of symmetrical common volume peak and large target return peak, Dalgleish et al., 2010a.	9
1.2	a.) LLS geometry with narrow IFOV receiver, b.) LLS setup with a wide IFOV Figure from Caimi and Dalgleish, 2013	11
1.3	Representive geometry from bistatic LLS system, also showing scattering events and laser-receiver FOV across unit area R_T . Figure from [1]	12
1.4	Illustration of a constellation of UMSLI transmitters illuminating a complete volume around an MHK device	15
1.5	Image of Barracuda as captured in clear conditions by UMSLI in the HBOI test tank for sparse and dense mode. Image of grouper taken in waters off Fort Lauderdale.	15
2.1	Schematic of UMSLI housing and components	18
2.2	Transmitter components	19
2.3	Ray trace and impulse response of PMT	20
2.4	CAD drawing of the receiver in glass sphere housing	20
2.5	UMSLI system control board schematic, main components include, Digitizer, Transmitter (Tx), and Receiver (Rx)	21
2.6	Profiler as deployed with configuration of UMSLI, SPLAT CAM, WBAT, AZFP	22
2.7	Map of cruise stations	23
3.1	Example of raw image waveform with ringing effect	29
4.1	Raw images from UMSLI system as greyscale splatted image	31
4.2	Ineffective attempt to exaggerate POI with increased contrast	32

4.3	Flow chart of processing steps for extracting POI	33
4.4	Splatted example image	34
4.5	Average background image slice	35
4.6	Image slice 7 with scaled return values	36
4.7	Distribution of return values across whole potential scale.	37
4.8	Left side of pixel return histogram with half Gaussian fitted curve. . .	38
4.9	Image slice 9, post threshold reveals POI for extraction.	39
4.10	Example of consecutive image slices with repeating particles. Red circle: example of ghosting caused by ringing in waveform of represented pixels; masking process removes these objects before evaluation of image slice. Orange rectangle: example of new particles still present after the masking process. Note: Other masked regions not marked.	41
4.11	Example image slice with extracted particle characteristics.	44
5.1	Downcast profile of Temperature (red) and density (blue) for station 5 and 6.	46
5.2	Particle counts from stations 5 and 6.	48
5.3	EK-80 acoustic time series.	49
5.4	Select PSDs from stations 5 and 6.	53
5.5	Cumulative PSDs from stations 5 and 6.	54

CHAPTER 1

INTRODUCTION

The ocean's mesopelagic zone is largely unexplored despite indicators that it plays a critical role in the ocean's ecosystems [2, 3]. The mesopelagic is the daytime home for organisms participating in massive diel vertical migrations throughout the world's oceans. Biomass in the mesopelagic is estimated to be 10 billion metric tons, accumulating to approximately 90% of the planet's biomass. The ambiguity and sheer size of this oceanic layer has led to little understanding of the organisms and their distribution throughout the water column [4]. Ultimately a lack of information about the mesopelagic has left the scientific community without data which helps model relationships to surface productivity, fisheries, and transfer of biomass in the ocean [3, 5]. To better understand this low light environment often coined the "twilight zone," the National Oceanic and Atmospheric Association's (NOAA) Cooperative Institute for Ocean Exploration, Research and Technology (CIOERT), based at Harbor Branch Oceanographic Institute (HBOI), has committed to a number of cruises in the Gulf of Mexico in order to test new technologies that shed light on this poorly understood habitat. The intention is to explore new and unique techniques that further develop our understanding of organism diversity in the mesopelagic, while also further comprehending biomass distributions, patchiness and migrations.

Our approach was to perform a number of profile descents with a diverse set of technologies that correlate in their sensing abilities. We combined several complementary acoustic and optical techniques to characterize distributions of organisms ranging from microbes to large nekton and small fish. Such instrumentation included an Unobtrusive Multi-Static Lidar Imager (UMSLI), Spatial PLankton Analysis Tech-

nique (SPLAT) bioluminescence imaging system, several optical proxy sensors, and multi-frequency acoustics. The mission of this exploration was to collect data on the distribution and dynamics of a multi-sized spectrum of organisms ranging from millimeters to meters, through the coherence of multiple technologies with overlapping ranges and spatial scales. On the large-scale spectrum, two multifrequency acoustic devices were deployed, the Acoustic Zooplankton-Fish Profiler (AZFP) and the Simrad EK80/WBAT; these instruments provide insight on mapping large-scale migration on a meter to 100's of meter scale. These acoustic devices detected real time migration from the depths of the mesopelagic to the surface as is often seen during the evening feeding hours. In the millimeter to meter range, the SPLAT camera system was employed for mapping kinetic interactions with bioluminescent organisms during instrument deployment through the water column. UMSLI, the primary instrument of this study, uses three-dimensional photo-realistic laser serial imaging for a wide range of applications such as detection, localization and identification. UMSLI outputs a traceable volumetric image that gives insight to environment interaction and distribution on a large scale. This study served to evaluate the obtained volumetric scans from the UMSLI system and develop a processing technique of data during the cruise to the mesopelagic.

The goal is to summarize the system's ability to observe a dynamic range of particles and extract quality images for feature analysis. This active system employs a narrow, highly collimated beam of light with complex optical arrangements. This implies concern for dependent sensor configuration and scene characteristics. We discuss the advantages of laser imaging, the nature of its development in the engineering field, and its basic principles and complexities. Often, cost and complexities discourage the use of laser imagers, however, for studying organisms in the mesopelagic the use of laser imaging holds many advantages in comparison to conventional underwater imaging which has several drawbacks.

Conventional cameras are a commonly used technology, but are limited by requirements that make it insufficient for undisturbed observation in the mesopelagic. Cameras with ideal setups depend on artificial illumination with large separation between the light source and the camera. As with all active imager systems, images are formed through the direct reflection of light from a target, but also consist of scattering along the propagation path from the source to the target, and ultimately the receiver. Scattering events of the light component that do not interact with the target are referred to as volume scatter [6–8]. It is this volume scatter effect that conventional cameras aim to avoid with larger separation between the light source and receiver [9]. Otherwise, as light propagates through a common viewing field, it scatters a number of times both before and after the target reflection as multi-scatter. To this effect, resulting images suffer from blurring and low contrast, making targets difficult to isolate from the background [6]. In high attenuation environments, conventional cameras are limited in performance unless alternative methods are used, such as high rate pulsating illumination and range gating [9]. Other limitations of conventional imaging systems are methods for resolving range and dimensionality of its target; without a means of recording transit time in link with the illuminator and receiver, there is a lack of parameters to determine the target’s depth.

Common observations reveal artificial lighting is also problematic when observing marine life. Multiple studies have shown unnatural lighting within a organism’s visible spectrum has behavioral effects, which consequently removes the opportunity to observe and record natural interactions [10–13]. The approach of active imaging is necessary in areas with little natural light; with the use of pulsating red diode lasers, we can avoid affecting behavior while still illuminating the target. Other technologies, such as acoustic imaging, stereoscopic imaging and holographic imaging have been developed to meet specific requirements with different levels of success.

Acoustic-related imaging systems are inhibited by spatial resolution and con-

trast due to naturally long wavelengths [14]. Sonar imaging of smaller organisms requires higher frequency instruments that are unideal due to the likely interaction of non-biological targets that give a false return. Other biological life found in the mesopelagic have a body composition that is largely aqueous and is difficult to detect with acoustic waves. Acoustic devices cover a large range, but provide insufficient physical descriptions of its target. Thus, for this study we still rely on acoustic devices for large scale observations, but resort to alternative methods for higher resolution imaging. Conversely, specialized optical imaging systems can provide higher resolution suited for more robust object identification, however, their use has been limited by hardware availability and platform size necessary for operation [14]. Recent advances in electro-optical sensors provides opportunity for laser imaging to be used underwater as an alternative imaging option in the fashion of lidar (light detection and ranging).

1.1 BASICS OF UNDERWATER LIDAR

From a general standpoint, lidar systems consist of two main components, the transmitter and receiver. The transmitter consists of a highly collimated laser, usually directed by a mechanical mirror device. The receiver may take many forms, but generally consist of a light receptor that quantifies intensity per unit area. Lidar signal is composed of an intense pulse of optical energy emitted by the transmitter, while a sample of the interaction of optical energy is recorded by the receiver. In a large sense, this is how all imaging systems function. Just as a conventional camera measures the backscatter of light off of objects in dependency to the source and receiver geometry, so does a lidar system. To further complicate the problem, the addition of an underwater environment creates housing and power supply restrictions, while adding a high attenuation medium. This section describes how engineering combats these challenges as we discuss the nature of using lidar imaging underwater

with performance enhancing techniques.

Lasers are capable of emitting light at very fast repetition rates with high energy levels. The collimated monochromatic nature of the beam makes it ideal for probing environments such as water. However, the interaction of light with particulates in the water greatly affects the nature of its propagation. The governing physics of light and attenuation plays a role in underwater sensing and is directly dependent on its ability for imaging. We define attenuation as the combination of absorption and scattering that adds to the total loss of light, as represented by the equation,

$$I(r) = I(r_0)e^{-c(r-r_0)} = I(r_0)e^{-(a+b)(r-r_0)} \quad (1.1)$$

such that c , represents attenuation, a , absorption and b , scattering of a propagated photon from the location r_0 to r [6]. As a laser transmits light energy through the scanned volume, the interaction of absorption and scattering between photons and particles take place as a likelihood determined by the medium’s Inherent Optical Properties (IOPs) [15,16]. In the case of absorption, a photon may not reach the receiver at all, thus, no information about the target is obtained by the receiver, which for the case of lidar leads to a loss of signal. Scattering can take many forms. Light that scatters in many directions distorts the propagation path of light, and consequently changes the radiant light field [1,7,17]. For this case, the photon continues towards the target on a now distorted path. When this happens, it is referred to as “single scattering,” or in the case of many scattering interactions is called, “multiple scattering.” These scattering events result to the fuzziness of obtained images. Numerical models show that photons are more likely to scatter forward in small angles, but again the scattering effect is dependent on the properties of the medium, and can scatter at any angle [18]. We also define the exponential loss of light in irradiance as it travels through an attenuating medium through the Beer-Lambert law as,

$$I_z = I_0 * e^{-kz} \quad (1.2)$$

where k , is the total attenuation coefficient, such that the beam irradiance will fall exponentially as a function of its distance $z = 1/k$. Photons that are not absorbed, but scatter forward to the target are reflected and are recorded by the receiver. Light-particle interaction is a complex field of study ranging from developing quantum level theory to more practical laboratory practices. The complete physical characterization of laser transmission is beyond the focus of this study, but is well summarized in the study of radiative transfer theory [6, 15, 16, 19–21].

The basis of lidar’s function is to actively illuminate a volume of water with a laser transmitter, and similarly with a receiver measuring irradiance as a function of time. The unique ranging aspect of lidar systems versus other active optical systems is defined by its time resolved ability to determine the range of a target from the resulting equation [22].

$$R = \frac{C * \Delta t}{2} \tag{1.3}$$

This stands as the fundamental lidar relationship between the range from a target given a known Δt , as the time of arrival (TOA); defined as the time it takes for a laser pulse to leave the transmitter, reflect from the target and return to the receiver. The sampling capability of the receiver defines the gate time and resolvable temporal resolution of the system. For lidar, we characterize a time dependent signal return as a function of the intensity of the light field, $L(r, \theta, \phi)$, at position r , in the given angle (θ, ϕ) , as the radiance measured per unit per differential solid angle [7].

Lidar uses the advantage of synchronous fields of view (FOV), collimated pulsating beams and range gating to mitigate the effects of unwanted scattering and maximize its ability to collect information from the receiver [1, 20]. It is intuitive to realize that this depends on the geometric relationship between the transmitter and receiver, as well the interaction that light has on particles in the environment, or in this case, water [23, 24]. There are numerous ways to alter the viewing apparatus of a lidar system as better explored in the coming sections, but generally, for all cases

the receiver coherently measures the backscatter of the volume illuminated by the laser transmitter [9]. Different lidar systems take different approaches to the FOV for the transmitter and receiver of the system, such as limiting the receiver to small viewing fields to minimize scattering. Other common approaches to lidar is restricting the instantaneous exposure time of the receiver to correlate with the transmitter emission [17, 25]. Studies show that increased transmitter-receiver separation and shorter pulse duration reduces common volume peak and mitigates scattering [21].

The lidar equation is the mathematical expression that represents the role of environmental parameters and systematic design in resolving lidar signal. The basic single-scattering equation for lidar is expressed as,

$$N(r) = \left[\eta(\lambda) \right] \left[\frac{A_T}{r^2} \right] \left[(P_A(\pi, r) * \beta_A(r) + P_m(\pi, r) \beta_M(r)) \right] \left[\exp(-2 \int_0^r (\sigma(r') dr') + B_D + B_S) \right] \quad (1.4)$$

where we define each term below with its corresponding dimensionality:

$$\eta(\lambda) = \left[\left(\frac{E_T \lambda}{hC} \right) \Delta r Q_E * T_O * O_A(r) \right]$$

$\eta(\lambda)$ describes the lidar performance and system specifications

λ is the laser wavelength (m)

h is Planck's constant ($J.s$)

C is the speed of light in the pertaining medium ($m.s^{-1}$)

Δr is the range bin length (m)

Q_e is the quantum efficiency of the detector

T_O is the optical efficiency

$O_A(r)$ is the transmitter and receiver FOV overlap

$P_A(\pi, r)$ is the backscatter function

$P_M(\pi, r)$ is the backscatter phase function

$\beta_A(r)$ is the volume scattering

$\beta_M(r)$ is the volume total scatter function

$\sigma(r)$ is the total volume extinction

B_D is the background signal due to thermal noise

B_S is the background ambient solar noise

The equation is presented in a way that breaks up the system's main components [22]. The first set of brackets denoted as the function $\eta(\lambda)$, consist of parameters specific to the lidar transmitter and receiver specifications. The second bracket represent the solid angle, $\frac{A_T}{r^2}$, and the scattering energy defined by the function, $P(\pi, r) * \beta(r)$. The third term includes the exponential loss of signal and describes the likelihood of attenuation of photons as it travels along its propagation to and from the transmitter and receiver. It should be noted that equation 1.4 is in its simplest form and only considers the single scatter case. Further derivation of the multi-scatter equation can be found in [26]. Further efforts to model these physical behaviors are undertaken by using Monte-Carlo and Small Angle Approximation methods [18, 27]. However, for the purpose of this study, the lidar equation is presented to point out important relationships associated with lidar imaging systems.

The intensity of the lidar signal is directly related to the number of photons as counted by the receiver. Figure 1.1 illustrates the effects of scattering on signal. The signal demonstrated above is a lidar signal without any presence of noise, but does exemplify the typical form of signal observed for underwater lidar. The red line represents a less desired signal that features multi-scatter caused by very turbid waters. This mitigates the target response which, is very small and could be lost entirely in the presence of noise in the signal. The initial peak present in the blue signal marks the common volume peak. The common volume peak represents the initial flux of energy caused by the intersection of the offset configuration between the FOV of the transmitter and receiver [28]. The downfall of the signal from the peak of the common volume represents the signal attenuating as governed by the inverse

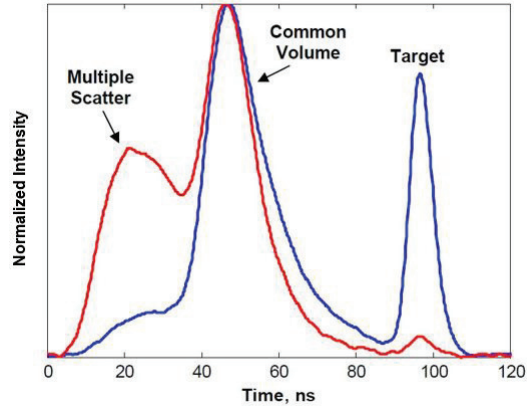


Figure 1.1: Time-series response of lidar signal: red waveforms represents multi-scatter case with small target return, blue waveform represent ideal case of symmetrical common volume peak and large target return peak, Dagleish et al., 2010a.

square of the range. Further analysis of lidar signal also shows that increasing the laser energy or field of view does not necessarily increase the lidar’s ability to detect its target. The power of the lidar signal exponentially decreases with distance, and most lidar systems rely on pulse accumulation and pulse interpolation techniques to increase the signal to noise ratio [9, 25].

Different lidar systems use different approaches to decrease attenuation of signal and increase dynamic range. Range gating, shortening pulse duration, high repetition rate, and frequency modulation, all increase the monetary cost and complexity to the imaging system [9]. We propose the use of a post processing methods that emphasize thresholding and statistical analysis of waveform returns to eliminate noise and resolve signal. As we shift this view to the case of lidar imagers, noise statistics become even more critical, and remain a key aspect of influence when evaluating underwater lidar signal.

1.2 UNDERWATER LIDAR IMAGING

Underwater lidar has many applications from localization, wireless communications and under more recent research, imaging [1, 7, 9, 14, 17]. This study focuses on laser imaging, a technique which involves the grid-like scanning of a defined volume with a highly-collimated laser source over a wide swath paired with a photon collecting receiver. There are a variety of methods used to extend laser imaging range, but all laser imagers are ultimately limited by beam spreading and attenuation. Here we present a brief history of the approaches HBOI has taken to improve performance of laser imaging as it pertains to the UMSLI system. Previous research at HBOI has focused its efforts to experimentation of multiple methods of laser imaging and continues to explore a number of prototype systems [1, 9, 13, 21, 23, 24, 28–33].

A common approach to laser imaging that is widely practiced is the technique of laser line scanning (LLS). Laser line scanning is described as using a collimated laser source to scan a narrow instantaneous field of view (IFOV) with a coherent narrow view receiver [1, 17, 29]. Synchronous LLS systems demonstrate scanning capability up to 70 degrees, usually with a continuous wave laser source. The laser is continually tracked on the target over a scan line by a narrow IFOV single element detector [1, 29, 34]. The transmitter mechanics of the LLS systems serially scans a target with a narrow FOV receiver, thus eliminating scattering due to the small evaluated areas. The range of LLS systems has been shown to extend further with a gated approach [19]. LLS systems for underwater imaging demonstrates a unique strategy for extending imaging range while also expressing the ability to extract three-dimensional details of its target [1, 19, 33]. Drawbacks of LLS systems include precise synchronization between the laser and receiver scan field and limited coverage area. The UMSLI system similarly uses the serial scanning technique to illuminate the water column in a line scanning sequence. We create a more reliable system by replacing the complex and less robust synchronously scanning receiver with a wide-

view staring receiver. Not to be mistaken as a LLS system, the UMSLI receiver does not synchronously scan a target area, but instead acts as a bucket photon collector. Figure 1.2 from *Subsea optics and imaging, chpt. 13* illustrates the difference in depth of field (DOF) and volume coverage for wide view and narrow view receivers for LLS systems.

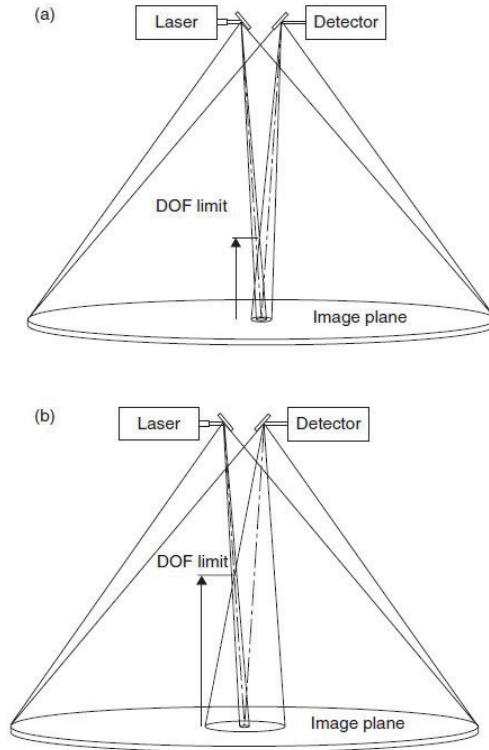


Figure 1.2: a.) LLS geometry with narrow IFOV receiver, b.) LLS setup with a wide IFOV Figure from Caimi and Dalgleish, 2013

Further advancement of study for LLS systems to improving underwater imaging was in testing the waveform effect of monostatic versus bistatic receiver setups for LLS systems in turbid environments. Just as image blurring becomes a concern for conventional imaging, lidar suffers from the effects of scattering in the commonly viewed field of the receiver and transmitter [4]. Transmitter and receiver geometry is a driving factor in lidar performance and shows direct implications on the outputted waveforms [24,35]. For narrow angular source and receiver apertures, we find

that imaging quality is more sensitive to random scattering inhomogeneities with a monostatic geometry. Figure 1.3 also from *Subsea optics and imaging, chpt. 13* represents the limiting effect of common volume scatter with a bistatic geometry. Results

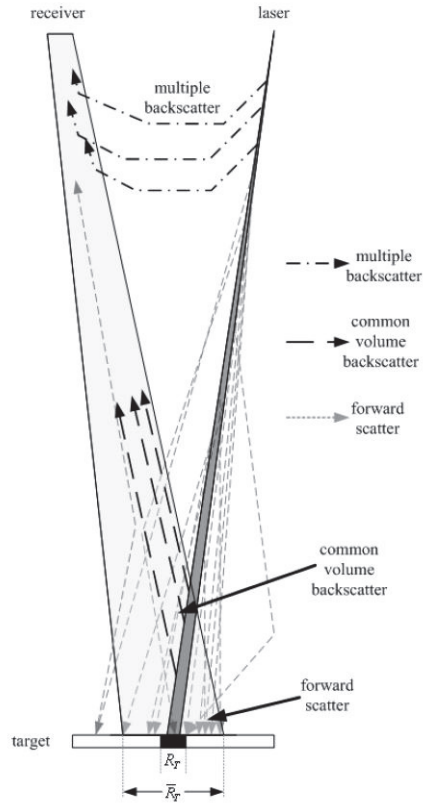


Figure 1.3: Representative geometry from bistatic LLS system, also showing scattering events and laser-receiver FOV across unit area R_T . Figure from [1]

have shown that increased transmitter-receiver separation with wireless synchronization through robust imaging links demonstrate significant improvements to image quality. However, bistatic setups restrict the imaging swath for serial imaging and multiple platforms are a restriction specific to imaging systems with large operation space [19, 28].

Development of laser imaging at HBOI experimented with using distributed serial imaging as an alternative to more traditional LLS methods. The distributed laser method included a 2-axis continuous wave scanning laser with a wide FOV high speed

receiver. Field experiments of this system found that the new hybrid system was able to resolve high contrast images over larger spans with limitations in overall range due to high attenuation [9]. Overall, the distributed laser system was able to create images at a much wider FOV and cover a larger target area [9]. This distributed imaging ideology is later used to progress the development of the UMSLI system. Acknowledgment during these studies all suggest post processing efforts are an efficient method to improve signal quality. Methods experimented during this study suggest that interpolating multiple samples over a longer time bin returned higher photon count per target pixel area, and multiple pulsating per temporal integration reduces system noise for acquired signals [24].

The UMSLI system is a composition of many of these previously experimented techniques that hold advantages and disadvantages. Similar success and results have been found by Neptec Technology Corporation and its commercial flash lidar system called LUCIE-3. The Underwater Time-Of-Flight Imaging Acquisition (UTOFIA) system as developed by the European Commission Horizon has a visual range of 4.5 attenuation lengths and recent publication shows promising results for image ranging and sizing [36]. The Electro-Optic Imaging model (EODES) by Metron Inc., has taken a quantitative approach to answering questions about radiative transfer and the effects of scattering and geometry on laser imaging performance [27]. Much of this progress is well summarized in Dalglish et al., 2013b. However, for all cases of lidar imaging we find the use of post processing methods are necessary to improve image quality and extract useful information.

1.3 DEVELOPMENT OF UMSLI

This method of laser imaging uses serially scanned pulsed lasers for extending imaging range in turbid seawater [1,9,31]. The approach to the development of UMSLI comes from the Marine Hydrokinetic (MHK) project. The impetus for the MHK

project was to develop a device that could unobtrusively monitor large marine life near underwater generators. The concern for marine life's interaction with the potentially dangerous equipment provides reason for a high priority regulator. Traditional methods of underwater surveillance instruments, such as cameras and acoustics, were disadvantageous because of the lack of efficient ambient light and need for high resolution and higher order dimensionality.

Sufficiently available underwater cameras require artificial light that would serve as an alternative, but were undesired because marine life is attracted to sources that emit light within their visible spectrum. To this regard, UMSLI uses a 638-nm wavelength red diode laser which is suitably below the maximum permissible exposure (MPE) limit for marine wildlife [10]. This makes UMSLI's laser invisible to marine life and allows it to unobtrusively make observations without affecting behavior. Unlike previously discussed laser imaging systems, such as LLS systems, UMSLI would have to monitor a large volume, therefore, a larger FOV and alternative sensing methods are necessary. UMSLI addresses these needs as a wide FOV imaging system that outputs time-resolved images capable of extracting three-dimensional features. Figure ?? demonstrates UMSLI's ability to observe a large sample volume around a underwater generator.

The need for an undisturbed, large volume surveillance system was the primary design component in the development of the UMSLI system for the MHK project. This type of design greatly relates to previous projects at HBOI that focus on near monostatic platforms, distributed lasers and imaging capabilities of lidar. To this regard, the UMSLI system was built with the intention of observing large marine species, as represented in figure 1.5. The adaptive nature of the UMSLI system has other applications.

The monostatic approach and dynamically expanding scan field make UMSLI suitable for resolving organisms of varying size due to an adaptive resolution featured

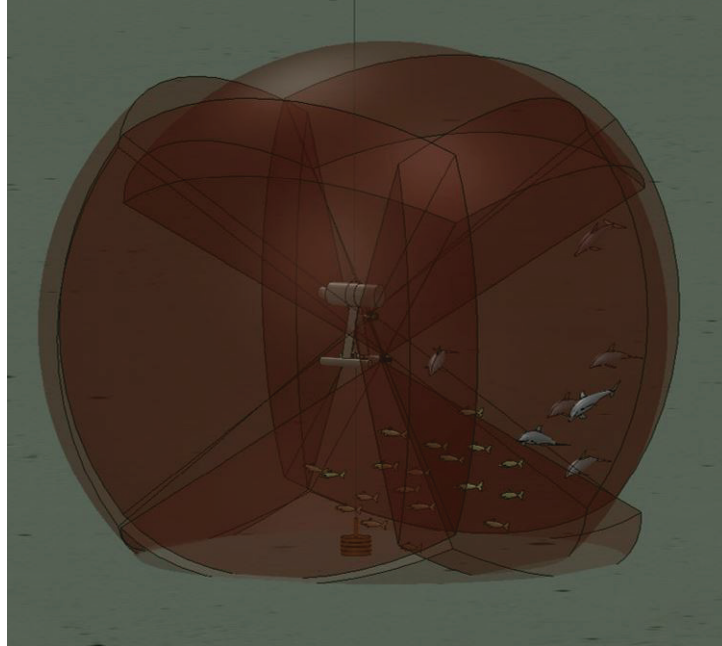


Figure 1.4: Illustration of a constellation of UMSLI transmitters illuminating a complete volume around an MHK device

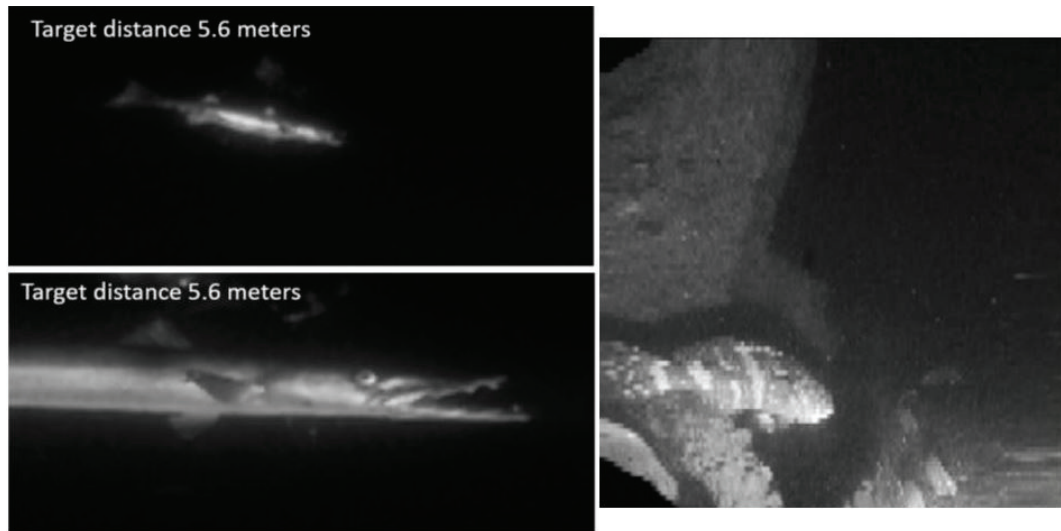


Figure 1.5: Image of Barracuda as captured in clear conditions by UMSLI in the HBOI test tank for sparse and dense mode. Image of grouper taken in waters off Fort Lauderdale.

based on the beam expansion of the laser during transmission. For this study we take a post-processing approach to extend the ability of UMSLI to observe much smaller organisms, such as small fish, krill and large flocs of marine snow. This effort extends

the UMSLI system's capability to resolve targets ranging from centimeters to meters with a depth of field range of 1-14 meters in the scan field. It is because of this advantage that UMSLI has been applied as a biological profiling instrument in the mesopelagic layer. HBOI has taken the approach of using lidar for observing diel vertical migration in the mesopelagic to evaluate suspended particle properties and conduct organism observations [16, 37].

The use of lidar for this exploration project is motivated by using its dynamic resolution and range to look closely at biological migrations that can not be observed with remote acoustic techniques. On the most recent deployment in the Gulf of Mexico, the UMSLI system was used with other optic and acoustic devices to profile and image biological migrations. This requires an alternative processing approach that aims to extract characteristics of smaller organisms, which defines the focus of this thesis. This processing technique includes signal filtering and thresholding techniques to extract images from the mesopelagic deployment.

CHAPTER 2

UMSLI SYSTEM AND EXPERIMENT SETUP

2.1 UMSLI CONSTRUCTION

UMSLI's concept of design is focused on surveying a large volume of water for the use of observation and identification of targets on a wide range of size scales (*mm*s to *m*s). UMSLI's main components includes multiple receivers (Rx), multiple transmitters (Tx), and a digital signal processor. The transmitters serially illuminate a volume of water by scanning a grid of pulses in a bi-directional raster pattern using an analog micromirror device (AMD) and a scan angle expansion lens. The scan field can be instantly configured to be either sparse or dense, concentrating a lower density pulse grid through a wider range of angles (sparse), or once an object is detected, concentrating a higher pulse density scan through a narrower range of angles (dense). The receivers consist of an 18 *cm* diameter sphere containing a pair of bi-directional red sensitive, high speed receptors. The volume scan field for each channel is maximized by an overlapping FOV region between the monostatic transmitter and receivers. The intent of the UMSLI system is to survey marine life. The system features a multi-static setup with multiple transmitters allowing for an object to be tracked across multiple scan volumes in a coherent direction.

The receivers, which consist of a high-speed photomultiplier module with focusing optics and a spectral bandpass filter, are designed to collect backscatter returns from the emitted laser pulses [11]. The returns are of either reflections from objects or scattering events in the backward direction. A high-speed digitizer and digital signal processor are then used to reconstruct the illuminated volume and output imagery

waveforms. These waveforms are then transformed and processed as a volumetric scan, with an $x - y$ spatial plane and a temporal z plane. Figure 2.1 illustrates the main design and geometric configuration of the UMSLI system.

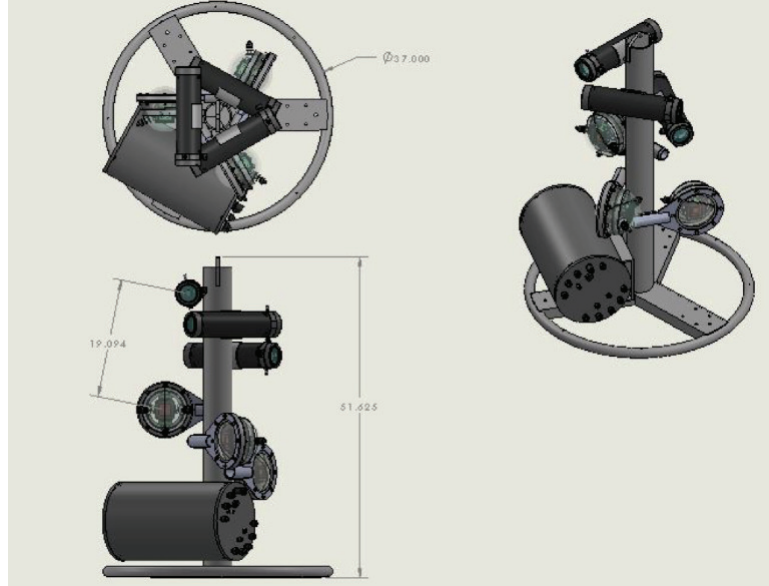


Figure 2.1: Schematic of UMSLI housing and components

Figure 2.2 shows the inside components of the UMSLI transmitter, which features a Sharp 638 nm red laser diode with a PICOIas laser driver that controls the voltage input as regulated by a transmitter controller board. A separate transmitter controller using RS-232 language communicates with the MEMS driver that adjusts the polar and azimuthal angle of a scanning two axis (tip-tilt) MEMS mirror (or "micromirror"). The MEMS mirror is mechanically responsible for the serial scan-like pattern of the system [11,32]. The reflected beam from the MEMS mirror is expanded using a small angle expansion lens that outputs a full beam divergence of 2.80 mrad in water. The beams radial intensity follows a circular Gaussian profile. The total scan angle of the volume, post beam expansion, emits over a polar angle of 0.9425 radians. For this setup, the geometry of the fully illuminated plane is consistent for both polar and azimuthal angles. The transmitter has a 4 ns FWHM pulse duration with an average power of 185 mW at a pulse rate of 80 kHz. The transmitter emits each

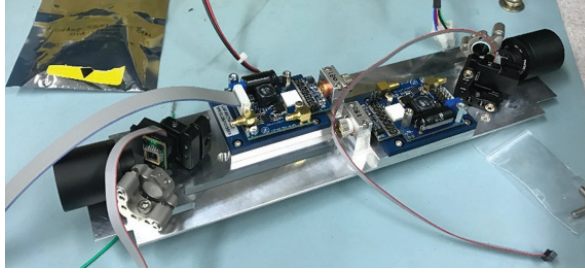


Figure 2.2: Transmitter components

pulse in a raster-like fashion that serially illuminates the volume of water, such that, the transmitter emits 200 lines that each consists of 200 pulses. Each line takes the transmitter 2.50 ms to complete, which allows the system to scan a full 200 x 200 plane in 500 ms for a total of 40000 pulses. The UMSLI system's adaptive viewing mode emits the same number of pulses at a smaller view angle of 0.3142 radians and 0.1047 radians. This allows for a high-resolution image in narrower views. It should be noted that the resolution for each image pixel is a function of the beam size as it expands in time, therefore, the dynamic resolution of the UMSLI system is configured in accordance to the beam spread.

The Photo-Multiplier Tube(PMT) receiver is responsible for mapping the light path from the transmitter to the target as received by a single element detector. The encompassing goal for this receiver design is to allow for a wide aperture FOV, while also restricting the PMT from exposure to light unrelated with the target's reflection. The particular PMT used for this system is a Hamamatsu R11265U series, type H11934-20. This PMT type has a spectral response from 300 nm to 920 nm, a quantum efficiency of 19% and radiant efficiency of 78 mA/W [38]. The temporal response of the PMT is the dominant restriction for the system response time. Figure 2.3 shows the rise time of the impulse response to be 1.3 ns and the fall time 5.8 ns. To eliminate any ambient light, the PMT has been capped with a rectangular light shield that concentrates the direction of received photons to only forward angles. The light shield design allows for a 30 degrees acceptance angle; figure 2.3 demonstrates

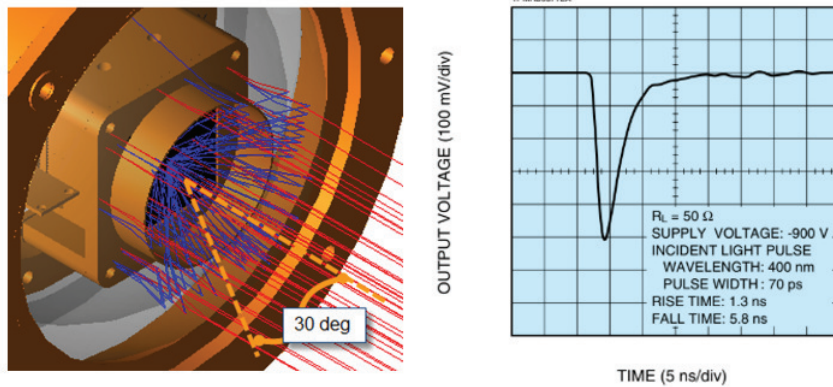


Figure 2.3: Ray trace and impulse response of PMT

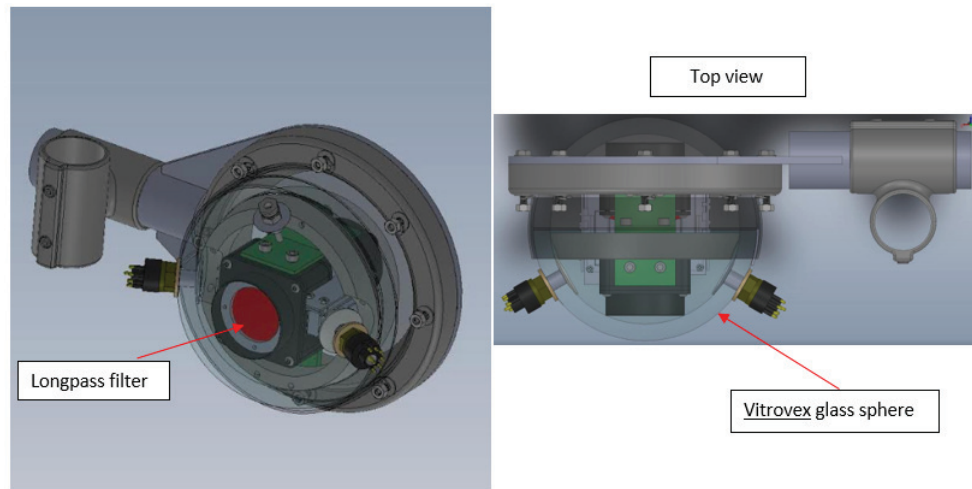


Figure 2.4: CAD drawing of the receiver in glass sphere housing

a ray trace of the light shield rejection pattern. Light that further enters the receiver travels through a glass prism, which is reflected into a Digital Micromirror Device (DMD). The DMD allows for further ambient light to be reduced before reaching a second prism and the PMT's photocathode plate. This allows for the rejection of unwanted photons, while desired light with correlating angles pass through to the PMT photocathode plate.

The last restrictions to the PMT's receptive spectrum are a Asahi Spectra long-pass filter and a microlouver film. The long-pass filter serves to eliminate any addi-

tional light below a 690 nm threshold, this ensures that the only light received by the PMT is from the transmitter and not an outside ambient source. The microlouver film contains small hair-like structures that limits the number of photons entering from perpendicular angles. The PMT and its components described above are housed in a Vitrovex glass sphere from Nautilus which are paired as two combined hemispheres sealed with Terrostat sealing tape. The 187 mm outside diameter glass housing has a total glass thickness of 14 mm and is pressure rated to a depth of 12,000 meters. UMSLI’s third primary component is the digitizer (Figure 2.5). It is responsible for

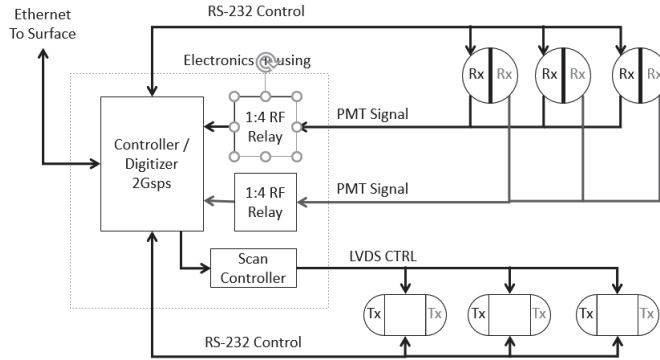


Figure 2.5: UMSLI system control board schematic, main components include, Digitizer, Transmitter (Tx), and Receiver (Rx)

sampling the illuminated volume and output waveforms of the illuminated areas of interest with a sampling rate of 2 GHz [13]. This surplus of samples is linearly interpolated into discrete time bins in correlation to the systems minimum pulse bandwidth of 5 ns and resampling rate at 400 MHz.

2.2 DEPLOYMENT SETUP

During March, 2018, the NOAA *Okeanos Explorer* navigated to the Gulf of Mexico to explore the mesopelagic region and monitor biological migration patterns. The UMSLI system was included on the exploration cruise with a number of other instruments. Collectively, these sensors served to measure the distribution of subsea

organisms as they migrate through the mesopelagic zone. The instruments included: the SPLAT bioluminescence imaging system, a AZFP, an IOP package, a Simrad WBAT sensor, and an acoustic EK-80 sensor that was hull mounted in the ship. These sensors (excluding the EK-80) were mounted onto an aluminum frame with dimensions of 1.8 x 1.2 x 1.7 (m^3) as shown in figure 2.6. The configuration of the sensors were optimized to minimize interference with each other and balanced to ensure a stable descent. Deployments were made at seven stations (figure 2.7) in the

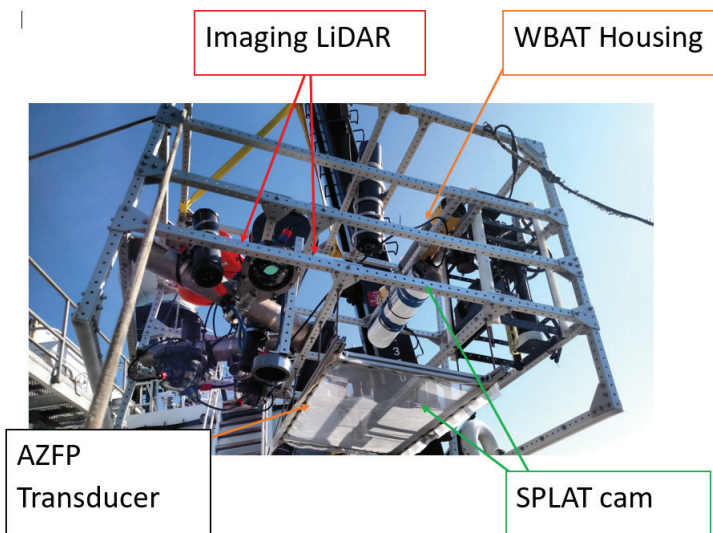


Figure 2.6: Profiler as deployed with configuration of UMSLI, SPLAT CAM, WBAT, AZFP

Gulf of Mexico over a five-day period. For each station, two deployment methods were conducted to characterize the water column and observe vertical migrations during key periods of the day. The first deployment for each station was a downcast from the surface to 300 meters. During the cast, select instruments profiled the water column throughout the profiler's descent. The second phase, following immediately after the downcast, was a time-series log at a constant depth of 300 meters. The time-series method allowed for a prolonged exposure of the water column that focused on the vertical migration patterns found in deeper scattering layers. During deployment, the EK-80 acoustic sensor on the *Okeanos Explorer* recorded live migration patterns

from the surface to 600 meters. These migration patterns were expected to involve descending organisms during the morning time-series and ascending organisms during the evening periods, according to literature [39]. The UMSLI system only collected

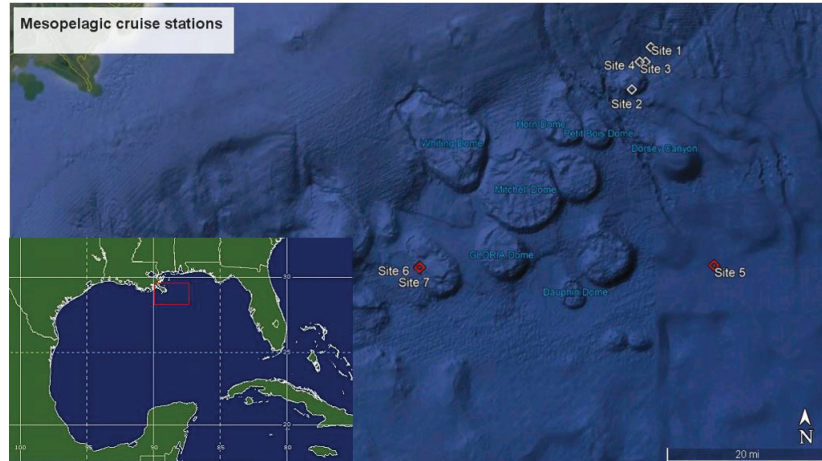


Figure 2.7: Map of cruise stations

data during the time-series deployments, sitting at a stable depth of 300 meters while scanning the water column. The UMSLI system took a sequence of 100 volumetric scans at each stationary depth, allowing for 100 scanned volumes of the water column to be recorded for analysis and comparison. The goal was to capture an abundance of samples at each depth, such that when the data is processed, the samples collected best represent the characteristics of the water column. The nature of the lidar setup plays a critical role in the methods used to analyze the data.

The UMSLI system was placed strategically at 300 meters in order to image large schools of small fish and krill as they were expected to move through the water column. The EK-80 allowed for live-view of the migration process and also confirms the upwelling of marine organism during the period of deployment. The UMSLI system served to provide higher resolution sensing with hope of images that give insight to the organism migration.

CHAPTER 3

DATA ACQUISITION

3.1 SYSTEM AND DATA CONFIGURATION

The UMSLI system relies on the active scanning and capture geometry between the transmitter and receiver to resolve information inside their shared FOV. Based on the setup during the deployment, the beginning of the shared cross-sectional FOVs between the transmitter and receiver starts at 1 meter, and continues outward orthogonal from the transmitter optical plane to a depth of field of 14.5 meters. The complete analysis of the signal is restricted to a maximum of 12.5 meters; beyond this the signal is insufficient to resolve due to attenuation. The receiver acceptance view expands horizontally and vertically in accordance to the 30 degree azimuthal and polar angles of the receiver. This expanding FOV covers 12 meters across in both planes (vertically and horizontally) at the maximum depth of field. The full volume which the UMSLI system observes and scans is approximately 664 m^3 .

We define the volume on a Cartesian plane, such that, the x and y axis, which we will refer to as the image spatial plane, is parallel with the face of the optical window of the receiver, and the z -axis protrudes outward perpendicularly into the water column. Because the transmitter emits the beam orthogonal to the z -axis, we can also say that the z -axis correlates with time (t). In accordance to the sampling frequency, the scanned volume is broken up into discrete time bins or "slices," as sampled by the digitizer at 2 GHz (256 time bins across 14.4 m). The PMT measures the backscatter of light temporally through the process of counting received photons that interact with the photocathode plate. Since photon detecting sensors use the

photo-electric effect to essentially regard photons as discrete energy packets, it is also valid to say the PMT measures the flux of energy across the time domain. Therefore, for each pulsed beam emitted in the z -direction from the transmitter, a temporal waveform of the beam's reflection is recorded by the receiver. Due to the proximity between the reflection of the beam and the adjacent receiver, we expect to see trends of larger signal returns during the early cross section of the commonly scanned volume.

For each volume scanned, the laser imaging system returns a $200 \times 200 \times 256$ (x, y, z) matrix of values. If we configure the volume into "binned" image slices, for which a slice represents the x - y dimension, then the volume is presented as 256 individual image slices. This is also comparable to a temporal view of the volume, at which the volume returns the time series of reflections of every beam in its path in the z -direction. For the analysis of each image slice, we only consider every other line in the y plane; this configuration is a correction factor for the jitter in the line scanning mechanics of the lidar. Such that, we compose a 200×100 pixel image in the x - y plane, while every pixel has a coherent temporal waveform sampled in accordance to the digitizer's sampling frequency. It should be noted that each pixel is defined as the illumination of the cross-sectional area of the collimated beam. This has several implications on the images rendered by this laser imaging system. First, the resolution of the pixel is a function of the beam's cross sectional area, and thus, the resolution of an individual pixel increases with distance due to beam spreading. The scanning grid and expansion rate of the beam for the UMSLI system was calibrated before deployment in the HBOI test tank. We assume a linear expansion in relation to the scan angle and depth of field. The location of each pixel spatially is a function of the cross track scanning mode of the beam's axis in the azimuthal angle (ϕ) and the polar angle (θ) as they pertain to the x - y plane. The offset location of each pixel is represented as,

$$\bar{x} = d * \pm \tan(\theta) \tag{3.1}$$

$$\bar{y} = d * \pm \tan(\phi) \quad (3.2)$$

for which,

$$d = \frac{(C * 0.5 * 10^{-9})}{2} * z_s \quad (3.3)$$

where $C = 2.25 * 10^8$ is the velocity of light in water, and d represents the depth of field as sampled by the digitizer (2 GHz) at sample z_s in the volume. Also, d represents the temporal resolution of samples in the z -direction. The expanding resolution ranges from approximately 1.27 *cm* per pixel at the nearest evaluated slice to 6.35 *cm* per pixel in the farthest evaluated slice. Other assumptions are made regarding to the beam's reflection from a target. Here, we assume that a target which returns a strong reflection from a single beam also characterizes the size of the beam at its point of reflection. This is a broad assumption considering that a particle much smaller than the beam's cross-sectional area can cause reflection, but this implication is essential to approximating the target size. We assume the system can only approximate a target size in accordance to the image resolution and ground-truth calibrated size.

3.2 NOISE CHARACTERISTICS

We classify the two major types of noise in lidar signal as random error and systematic error. Random errors are caused by uncontrolled physical processes in the environment and electronic components. This includes thermal noise in the signal and speckle in the images cause by scattering. Systematic noise is a causation of miscalibration and mechanical faults that pertain to user error. Though it is difficult to remove systematic noise without investigation of the source, random error can be mitigated if isolated properly. We attempt to remove noise from the PMT sensor and digitizer that make up the main components responsible for added random error [40]. Thermal noise adds a random zero-mean white noise to the signal, when isolated this type of noise is described to have a Gaussian distribution [11, 41]. This Gaussian

noise is represented by the probability density function below.

$$N(x, \sigma) = \frac{1}{(\sqrt{2\pi}\sigma)} e^{(-x^2/(2\sigma^2))} \quad (3.4)$$

The PMT itself measures the process of counting photons that interact with the photocathode plate and are multiplied inside the photo-multiplier tube in dependence of the set gain factor [42]. The counting of photons as individual events is an inherently random physical process which follows a Poisson distribution. This leads to the signal dependent noise component referred to as shot noise. Such that, the number of photons received by the sensor element over a period, T , is characterized by the Poisson probability distribution below.

$$P(k, T) = \frac{(\lambda)(T^k)(e^{-\lambda T})}{k!} \quad (3.5)$$

λ is the average number of photon events per second over k events, and $(\lambda)(T)$ corresponds to the expected incident photon count. It should be noted that the Poisson distribution is a single parameter distribution that is dependent on the signal. The energy per photon is represented as $E = nhv$, where v is the carrier frequency, h is Plank's constant and n is the number of photons. For the case of the Poisson distribution, the ratio of standard deviation to the mean is represented as $\frac{1}{\sqrt{n}}$ where, $n = \lambda T$, which represents the number of photons received over an observation period [42, 43]. Through this process, shot noise grows with the square root of observed photons received [43]. This also implies that the signal to shot noise ratio is exaggerated with the capture of more photons, and longer exposure times [25].

Under many assumptions with image noise, the additive noise to the signal is independent [43]. Under this imaging system, there is an underlying thermal noise that is independent of the signal, however, there is also an added shot noise that is dependent to the signal and varies in accordance to pixel intensity.

For this case, let us consider a dependent signal for any pixel $x \in X$ where X is the domain of the scanned volume within R . R represents the spatial domain of the water column. Such that, $\tau : X \rightarrow R$ is the recorded signal, also $y : X \rightarrow R$ is the unknown signal, $\varepsilon : X \rightarrow R$ is the systematic noise and σ is dependent to y , that gives the standard deviation of the systematic noise component [44].

$$\tau(x) = y(x) + \sigma(y(x)) * \varepsilon(x) \quad (3.6)$$

We can also say that the mathematical expectation of the independent systematic noise of the signal, $E\{\varepsilon(x)\} = 0$, and $E\{\tau(x)\} = y(x)$ to be defined as the noisy signal observed [42]. Because we define our signal-noise components as both dependent and independent of the expected signal, we break up the Gaussian signal and Poisson dependent signal, as such,

$$\sigma(y(x)) * \varepsilon(x) = \eta_p(y(x)) + \eta_g(x) \quad (3.7)$$

Where $\eta_p(y(x))$ is the Poisson distributed noise and $\eta_g(x)$ is the Gaussian zero mean white noise, as presented above [44]. Such that, $\eta_p(y(x)) \sim P(y(x))$, $\eta_g(x) \sim N(0, \sigma)$. We see from equation 3.5 that the photon counts directly affect the variance of the Poisson distribution, hence, the reason for its dependency [41]. For larger photon counts, such as $n \rightarrow \infty$, the Poisson distribution closely relates to the Gaussian distribution in accordance to the central limit theorem [42, 43]. It is for this reason, shot noise in cases of longer exposure times is modeled as a zero mean Gaussian distributions [44].

A signal anomaly that is apparent when looking at signal from the PMT receiver is the case of photoelectric ringing. This anomaly occurs when the PMT photocathode plate receives a surplus of many photons in a short duration, and as a result, saturates the returned signal [45]. In this case, the sensor releases electrons at random during the PMT response fall time and the result is a residual false return ringing in the temporal waveform. This presents the problem of false particle counts; as a preventive

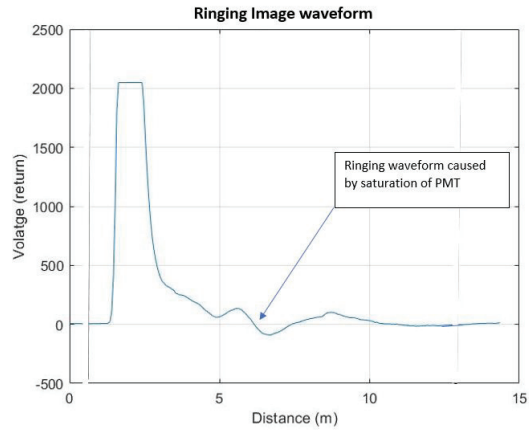


Figure 3.1: Example of raw image waveform with ringing effect

measure to this, a spatial image mask is used to prevent this measure as discussed further.

CHAPTER 4

PROCESSING METHODS

Here, we present a threshold and extraction method for imaging lidar that evaluates volumetric data for particles of interest (POI) suspended in the water column. We define POI as organisms or objects which give a statistically large waveform return above common noise values. For the data collected from the mesopelagic cruise, we expect to resolve POI with a wide range of size and shape, though the expectation is that most POI fall under the category of large nekton, small fish, and larger accumulations of marine snow. The reader should note that typically the term particles refers to much smaller objects in the water column, though here we use the term particle, objects or POI loosely as we observe a wide range of size classes.

The focus of the presented methodology is to create an adaptive threshold technique that evaluates each set of scanned image volumes without prior knowledge of environmental noise characteristics. The determinate thresholding step is critical to the binarization of volume slices and the selection process of extracted POI. Our strategy for extracting objects is not focused on a single size group, although the study could be limited to a focus group of larger organisms or smaller particles, as this would in effect subtly change the threshold steps chosen below. Our thresholding approach uses statistical means in the temporal case and is adaptive to the dynamic background and resolution of the volume field.

Lidar volumes are also presented as raw "splatted" images. Splatted images consist of the returns of the first half of the capture volume combined and re-scaled as a greyscale image. Figure 4.1 gives examples of splatted images with notable POI present. Splatted images give an overall idea of whether the volume scans contains

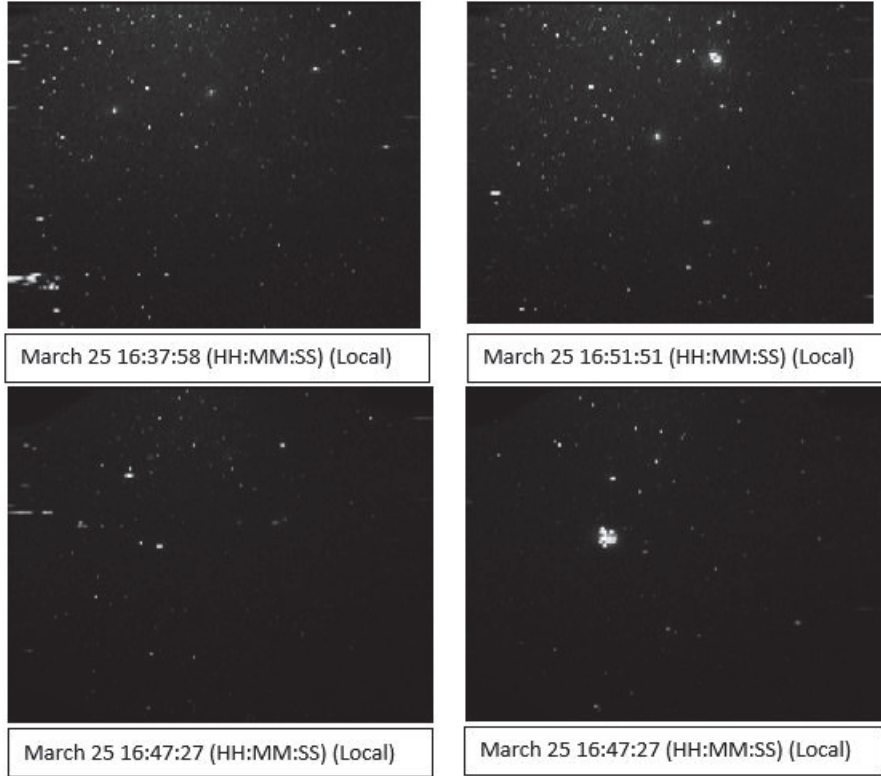


Figure 4.1: Raw images from UMSLI system as greyscale splatted image

POI as a form of validation. However, due to scattering and shot noise, some particles are difficult to distinguish from background speckle with the naked eye. Also, objects in the splatted image are not scaled to the ground truth size, meaning objects that appear in early sections of the volume may appear as large as objects further in the background despite their actual size. Furthermore, the image noise adds a fuzziness to the image, and ambient light towards the top left corner of the image creates an uneven background. Random speckle in the background is difficult to distinguish as POI or as undesired smaller scattering returns. A simple image processing approach to greyscale images would be to apply smoothing filter and contrast enhancement [30]. For the case of lidar signal, noise is a dependent aspect of the signal (defined in noise characteristic section), we find that contrast enhancement methods are ineffective, as is apparent from figure 4.2. Smoothing methods, are ef-

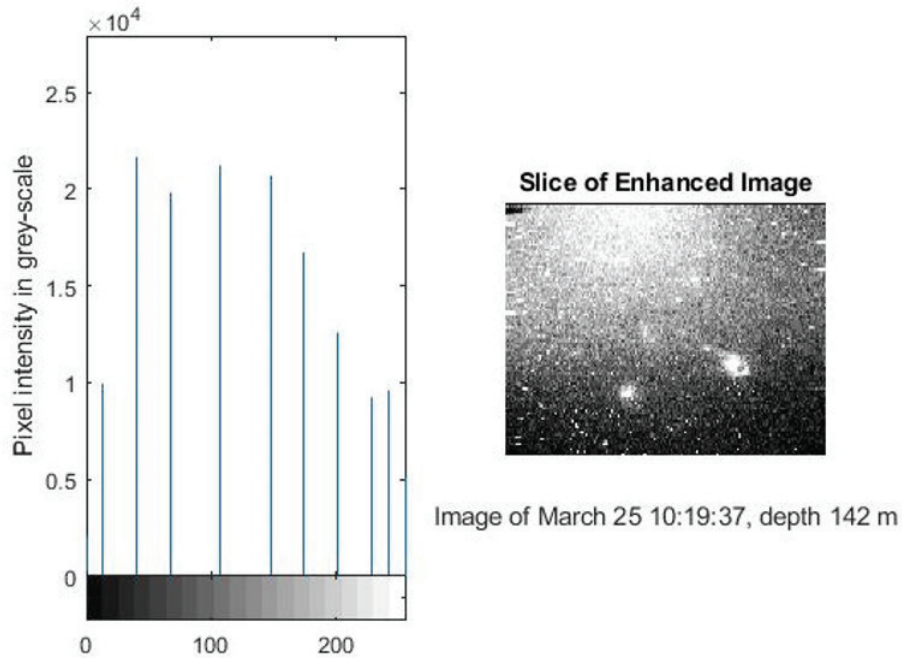


Figure 4.2: Ineffective attempt to exaggerate POI with increased contrast

fective for distinguished images of larger objects, eliminating smaller particles that hold statistical significance.

Another image processing approach was through frequency analysis. This method considers the power spectral density of a single lidar waveform which contains a significant return. The goal of the power spectral estimation is to isolate the band of frequencies that contains the majority of the signal. We wish to resolve a wide range of particle sizes, therefore, cannot focus on narrow bands of frequency. We find in this analysis that the power of the lidar signal is very wide spread across many frequencies, and that simple cut-off frequency methods result in a loss of signal containing particle returns [40, 44, 46]. During the processing of the lidar images, the method presented below served better than the approach of digital frequency and image smoothing filters. The flow chart presented in figure 4.3 steps through the post processing methods taken to resolve POI from the volumetric data. We will use an

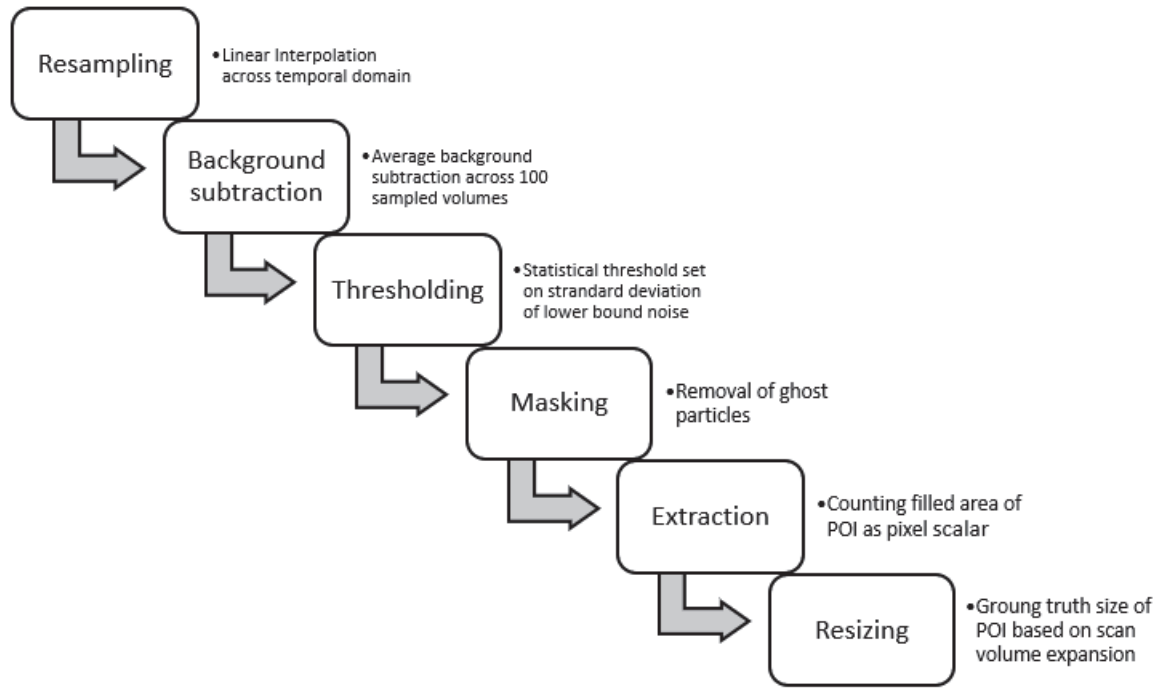


Figure 4.3: Flow chart of processing steps for extracting POI

example volume scan from station 6 captured at time 17:47 on March 25th at a depth of 300 meters. As we step through the processing methods for the UMSLI system the image presented in figure 4.4 will be used as an example for the remaining figures for this chapter. As shown above, this example image is a splatted image of the first half of the volume, though we will process only the first slice of the image completely, many of the POI are notable.

4.1 RESAMPLING

The first step in evaluating each volume scan was to perform a cubic spline linear interpolation for each of the returned temporal waveforms in accordance to the PMT bandwidth of 400 MHz. The interpolation step is conducted across each waveform independently as represented by each pixel in the time domain [47]. To this effect, the newly configured data is resampled into 52 discrete points of return in the signal.

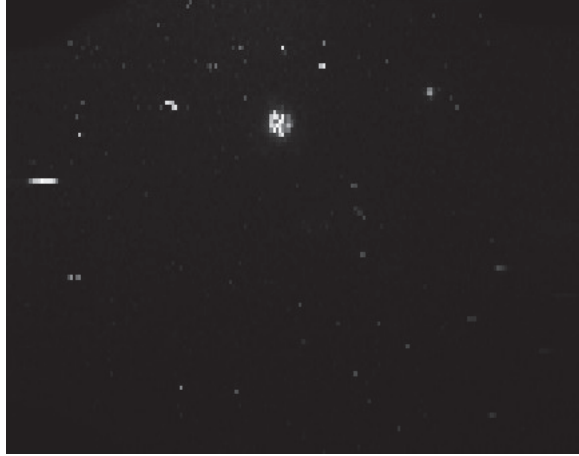


Figure 4.4: Splatted example image

This method is a common lidar approach, as sampling multiple pulses over a longer time duration, reduces speckle and overall increases signal to noise. [19, 25, 40]. As a trade-off we are increasing the bin length of each sample and therefore, capture a larger section of volume as a discrete volume slice. This method does decrease our temporal resolution, but in effect greatly reduces noise in the spatial domain of the image. For the newly evaluated waveform, the cut-off samples of the signal begins at the newly sampled 9th slice and ends at the 45th slice. Data before the 9th sample point is before the full FOV intersection of the laser and receiver and holds no significant information, while signals after the 45th sample point are too low to resolve due to attenuation.

4.2 BACKGROUND SUBTRACTION

To eliminate data offsets and remove noise apparent from the background, an average of 100 individual volume scans were subtracted from each volume sample. This gives a statistically appropriate number of samples over a short period of time that represents the expected background of each volume. As stated previously, at each sampled depth, 100 volume scans were sampled consecutively. The background

subtraction serves to reduce variation in intensities across the temporal slices in the volume as well, account for the spatial characteristics in the signal [40]. To this regard, temporal noise that appears to be largely shot noise dominant early in the signal is reduced, while spatially uneven illumination and background ambiance is dampened.

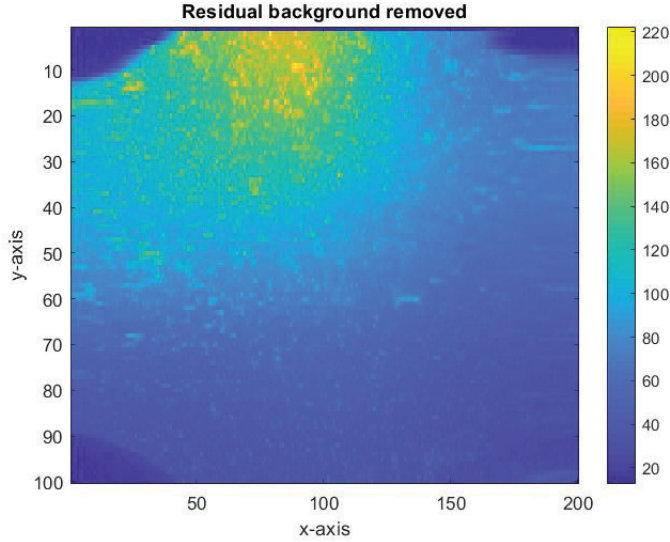


Figure 4.5: Average background image slice

Figure 4.5, shows a intensity plot of the residual intensity of an average background volume slice. Here we display the 9th sample slice of the average background from the raw volume data, revealing the spatial characteristics of the noise in relation to the transmitter and receiver geometry. In monostatic lidar layout, we witness high signal returns on the volume plane closest to the transmitter. As is apparent in the figure, the top left corner on average reflects higher return intensity. The background subtraction method is a correction factor for this uneven power distribution. Since signal is lost as the laser propagates through the water, we observe more signal in the earlier sections of the volume. However, the signal noise dependency creates a larger variance of noise in sections of the volume with higher average returns. Image slices have a large range of pixel intensity values ranging from 2000 to -50. The result from

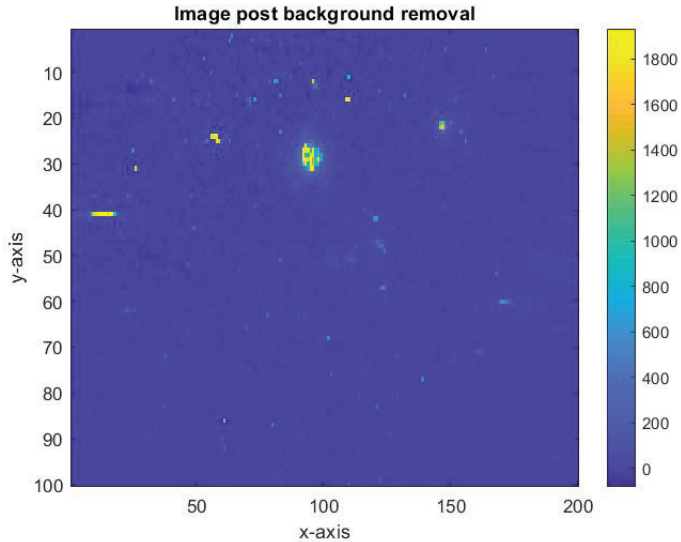


Figure 4.6: Image slice 7 with scaled return values

negative values are from the pulse ringing and are described in the previous section.

Going forward, we focus on the volume slices rendered as images. Figure 4.6 shows the 9th volume slice from a scan volume after the background subtraction. The volume slices are treated as single images, though they actually represent the signal return as observed by the PMT during the time bin designated by the impulse response of the receiver. This image slice is used as an example because it contains both large and small particles. Also, we use the 9th slice because it is the first evaluated slice in a volume and typically returns more particles due to a higher signal intensity. It should be noted that earlier sampled slices contain the sections of lidar waveform with higher intensity, while slices further in the volume have lower returns. This creates a large variation of return values that vary greatly depending on their distance from the transmitter. This makes an adaptive threshold imperative when we consider each image slice individually. The next step in the data processing is to determine what range of return values for a particle constitutes it as a POI and what returns are considered environmental noise.

4.3 THRESHOLDING

Our approach for determining an optimal threshold for image slices is to evaluate each temporal slice independently. This method was chosen due to the large variation in background intensity across the temporal domain. Though the average background subtraction removes much of this effect, we still consider the returned signal to carry a statistical variation due to its noise dependence and the exponential loss of signal. The remaining signal is represented as a histogram of pixel intensity returns for an image slice. As seen in figure 4.7, the majority of the returns are centered around zero, and show characteristics of white Gaussian noise. We see that a large portion of the

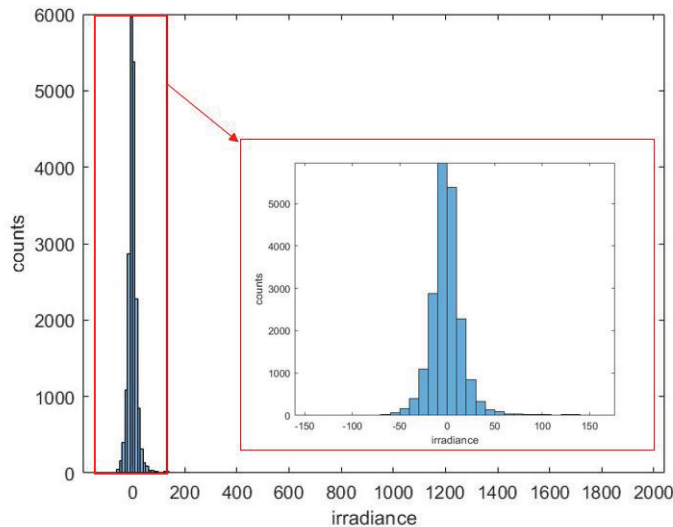


Figure 4.7: Distribution of return values across whole potential scale.

return values fall on the low end of the intensity spectrum. This is expected because of the obviously dark background, our concern is what we characterize as a particle. We expect a low end distribution to represent the noise floor of the image slice. The pixels with values close to zero we characterize as pixel values of insignificant returns and assume they are least probable to be POI values. MATLAB presents multiple automated binarization methods of images through the isolation of background and foreground pixels [48, 49]. Most of these methods, such as Otsu's method, segments

the image pixels into classes of foreground and background and choose a threshold that minimizes the intraclass variance of the thresholded black and white pixels. This method requires a more defined double mound histogram between lighter and darker pixels, and is less effective with images containing smaller objects [48,49]. As shown in figure 4.7, the lidar images do not have a defined foreground and only contain a very obvious background peak [48]. To determine image slice thresholds, we set a boundary cutoff value based on normal distribution statistics of the noise floor as represented by the lower bound peak. This is to ensure our threshold value is as close to the noise floor as possible to maximize the number of resolved particles, while still eliminating the computation of false POI.

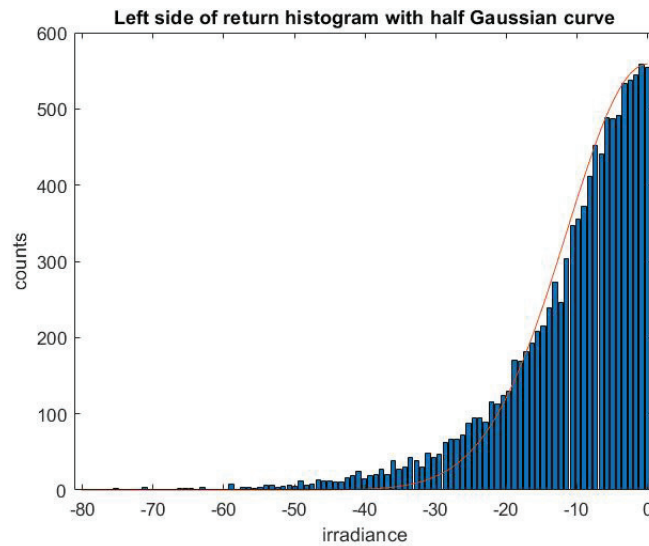


Figure 4.8: Left side of pixel return histogram with half Gaussian fitted curve.

After isolating the left side values of the noise floor (figure 4.8), a half Gaussian curve is fit to the left side of the bin points using a least squares error function. The statistical definition of the half Gaussian curve gives reference to the lower bound noise of the histogram. The standard deviation of the Gaussian curve is used as the basis for setting a threshold value for turning each image slice into a binary image that only contains POI. This threshold is based on the standard deviation of the lower bound

histogram of each temporal image slice. Henceforth, we define the optimal threshold value as $5 * (mode + 3 * std)$. The extra scale factor was found as the value that best prevented the counting of false POI and is justifiable based on the large dynamic range of the lidar waveforms. From this process the returned threshold serves as a cut-off value for the binarization process of each image slice. Values greater than the threshold in the slice are kept and considered POI, while returns lower are neglected and set to zero.

When evaluating the image post threshold in figure 4.9, we see that pixels previously hidden in the background are extracted. As a result of high reflection from

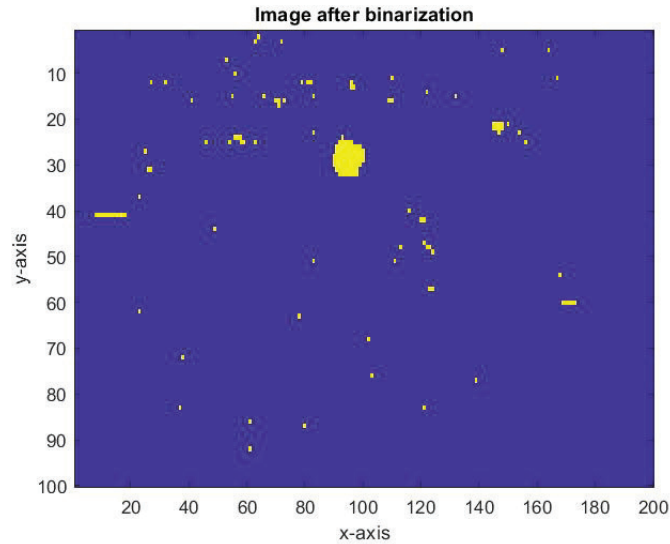


Figure 4.9: Image slice 9, post threshold reveals POI for extraction.

larger particles, we witness a halo effect in the resolved image. We expect that larger POI give saturated signal return in the pixel waveforms are over estimated in size. This overestimation we predict to be an effect of higher returns due to scattering caused by initial reflection from highly reflective objects or close proximity to the receiver. Efforts to eliminate this effect were explored but not resolved and further research of water-shedding techniques are still being considered [50].

4.4 MASKING

As previously mentioned, when the PMT receiver records a large number of photons, the returned signal will have a ringing effect. This ringing anomaly for select cases causes the same particle to appear in multiple image slices. In order to prevent an inflation of particle counts, we apply a binary mask to each image slice in accordance to the slice before it [50]. The binary mask compares each counted pixel and compares it to the previous slice. If the two slices share a pixel at the same address, then that pixel is removed from the current evaluated slice. This method assumes that two particles cannot exist in consecutive slices, and the masking method is a preventive measure from counting particle returns for the remaining volume. In order to compare consecutive slices we use a binary subtraction method. Consider the simple 2 x 2 identity matrix, which we say represents as a 4 pixel binary image, such that a zero signifies a background pixel and a one is a counted pixel. We will call this the first slice of the volume.

$$\begin{bmatrix} 1 & 0 \\ 0 & 1 \end{bmatrix}$$

Similarly, we can identify the second slice as the matrix.

$$\begin{bmatrix} 1 & 0 \\ 1 & 0 \end{bmatrix}$$

For the first slice of the volume we assume there are no repeating particles and can evaluate it normally, however the following slice we compare to the slice before it to identify a repeating particle. To evaluate the 2nd slice, we multiply the previous slice (1st slice in this case) by a factor of two and then subtract the current slice as demonstrated.

$$\begin{bmatrix} 2 & 0 \\ 0 & 2 \end{bmatrix} - \begin{bmatrix} 1 & 0 \\ 1 & 0 \end{bmatrix} = \begin{bmatrix} 1 & 0 \\ -1 & 2 \end{bmatrix}$$

Thus, we can identify the 4 possible outcomes where: a return value of 1 is a repeating pixel that should be masked, 0 is counted as a repeating background pixel, -1 is a newly counted particle for the evaluated slice, and 2 is a previously counted pixel from the first slice and is disregarded. When comparing the 3rd slice, the 2nd slice takes its original form as it is presented before being masked itself. If a particle continuously appears in three slices, it will still be eliminated by comparison of the original second slice, thus again eliminating the reoccurred particle across multiple slices. In this morphological approach, if a particles occupies a pixel address, it is not counted for the remainder of the volume. This process is further exemplified in figure 4.10.

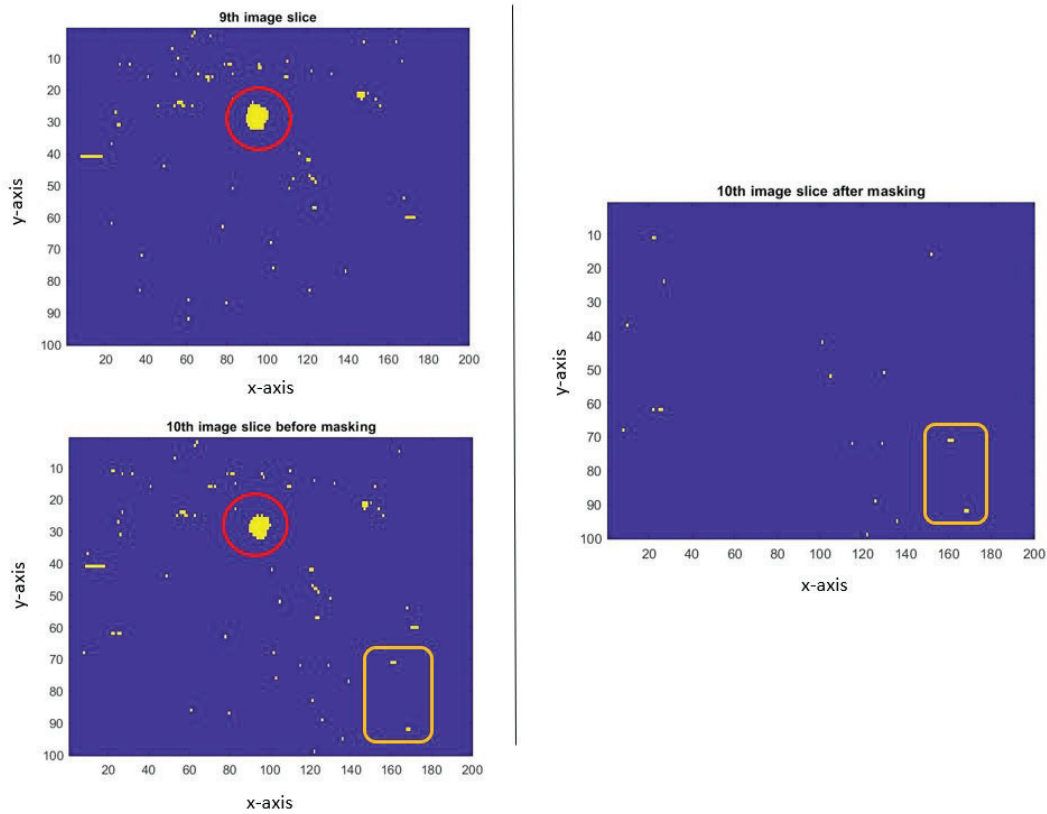


Figure 4.10: Example of consecutive image slices with repeating particles. Red circle: example of ghosting caused by ringing in waveform of represented pixels; masking process removes these objects before evaluation of image slice. Orange rectangle: example of new particles still present after the masking process. Note: Other masked regions not marked.

For each pixel masked, the remaining volume that it occupies is subtracted from the whole, we find in the results that the ringing waveform is an anomaly, and only occurs during cases of saturation of the PMT. The calculated volume subtracted due to the masking process, is continuously less than 10% of the total volume.

4.5 EXTRACTION AND RESIZING OF POI

After the masking process, the binary image slices contain only POI as remaining white pixels. From these images we extract information about size and shape of the POI using image processing tools from MATLAB. These include the major and minor axis lengths and "filled area" of the pixel regions. The major and minor axis length is measured as the per pixel count of the major and minor axis of a set of connected pixels that has the same normalized second central moments as the pixel region. From the major and minor axis length, we calculate the aspect ratio of each POI. The filled area returns a scalar number of pixels that make up a POI region, where the region is defined as any number of pixels connected adjacently to another. If the pixel region encloses an area with consecutive connected pixels, then the filled area includes the holes of the pixel group. We define the filled region as the cross sectional area of the particle of interest, we assume evaluated POI to be a sphere [50]. We found this approximation to be acceptable as the aspect ratios reveals the pixel regions to be dominantly 1:1.

After the cross sectional area of each pixel region is counted, the particle is resized to the ground truth size of each image slice in accordance to calibration measurements taken before deployment. Also, calculated is the total volume scanned with the masked volume removed and the thresholds calculated for each image slice, as shown in figure 4.11 and table 4.5.

Major Axis Length (pixels)	Minor Axis Length (pixels)	Filled Area (pixels)	Mean Intensity	Min Intensity	Major Intensity	Calculated Diameter (cm)
11.00	8.56	72	819.28	173.01	1913.15	12.16
12.70	1.15	11	1593.18	227.17	1931.70	4.75
4.43	2.88	9	762.25	172.59	1603.67	4.30
4.49	1.72	5	1898.52	1871.05	1912.03	3.20
5.77	1.15	5	423.00	217.42	655.30	3.20
5.36	1.38	4	389.91	327.97	483.57	2.87
2.58	1.76	3	800.44	182.06	1851.74	2.48
2.58	1.76	3	272.00	193.25	381.97	2.48
3.05	1.15	2	568.93	546.08	591.79	2.03
2.30	1.15	2	643.33	493.31	793.35	2.03
2.30	1.15	2	1891.03	1881.03	1902.91	2.03
2.30	1.15	2	1021.77	175.45	1868.10	2.03
2.30	1.15	2	606.94	603.75	610.13	2.03
2.30	1.15	2	486.69	450.70	522.68	2.03

Table 4.1: Table of POI characteristics from figure 4.11

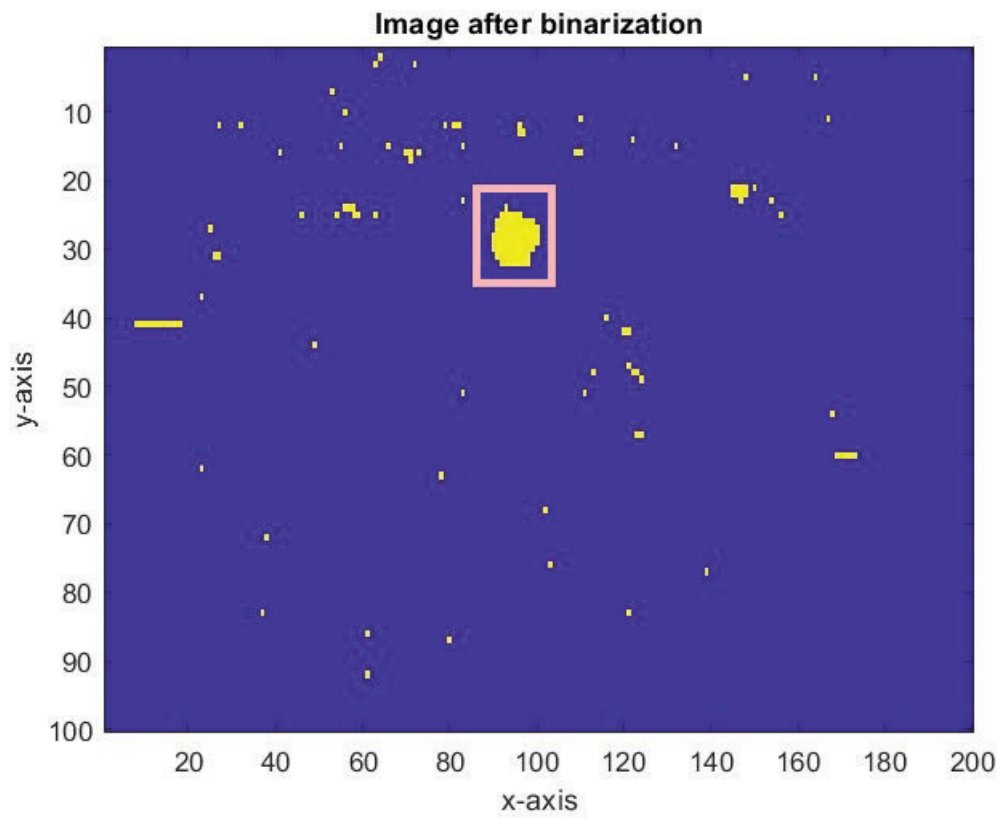


Figure 4.11: Example image slice with extracted particle characteristics.

CHAPTER 5

RESULTS AND DISCUSSION

The data sets shown in this chapter are from two stations during the mesopelagic cruise. The focus of the data presented is from stations 5 from 5:00-7:00 and station 6 from 17:00-19:00, both on March 25, 2018. For both stations, we characterize the water column using CTD data from the downcast deployments, and examine data captured during extended time-series deployments. We aim to make observations for particles counts and particle size distributions (PSD) that characterize the mesopelagic zone during prime migration periods. Using the methods outlined above, we process the data set and present results that both validate protocols that provide insight in characterization of extracted particles. From the lidar data, we demonstrate the fluctuation of particles counted in time as it relates to the migration patterns observed. The presentation of PSDs gives insight on size distribution and abundance, however, it does not include detail about the identification of these particles. We recognize the original purpose of the UMSLI system is for identification. The aim here is to test a new method to extract particle characteristics, such as shape, size and spatial proximity. We expect distributions with relevance to a large range of organisms, floc aggregations and particulates alike. This chapter interprets the results rendered from the methods described above, as it pertains to the processing steps and the assumptions used.

5.1 WATER COLUMN PROFILE

Figure 5.1 shows the CTD data for stations 5 and 6, which depicts the temperature and density measurements taken during the downcast before the time series deployments. For both stations 5 and 6, the decrease in temperature and density follows a similar slope from the surface to 100 meters. There is a steep decline in temperature down to 100 meters indicating the presence of a thermocline and halocline. The slope for both stations shows a more gradual decline as it approaches the sampling depth of 300 meters. During the time series scans for both stations 5 and 6, the temperature was consistent, only varying a few degrees throughout the recording. We expect the water characteristics for station 5 and 6 to vary considering their spatial differences and levels of biological activity in proximity to the Mississippi delta [39].

Station 5 (5:14-5:25) and 6 (16:38-16:49) CTD Downcast

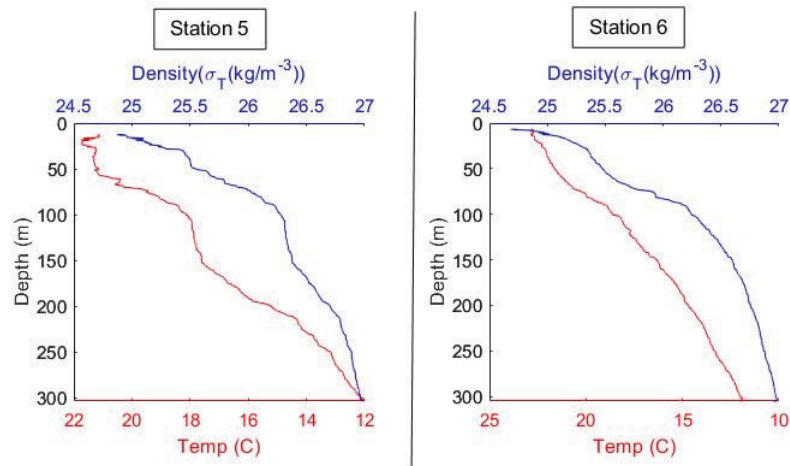


Figure 5.1: Downcast profile of Temperature (red) and density (blue) for station 5 and 6.

The time of the sampling at both of these stations also varied. Station 5 samples were taken during the early morning, while station 6 samples were taken in the late evening. These sampling periods are critical to the expected migrations of marine organisms with respect to the particle size range of the lidar. We expect a rise and

fall of particle counts in correlation with the migrations periods, and assume that during periods of little activity, the particle counts remain stable. We also consider the aggregation stages of marine snow as it pertains to the bio-activity to the euphotic layer above, as we expect its abundance to be a constant background.

5.2 PARTICLE CONCENTRATIONS

Figure 5.2 presents the particle counts for station 5 and 6 as a stem plot. Each stem represent a lidar sample that contains 100 consecutive volumetric scans, each sample set is captured at 5 minute intervals. The particle count for each sample represents the sum of all size class POI resolved from the volumes during the sampling period. For station 5, 1800 volume scans were processed, these scans spanned approximately from 5:15 to 6:33 local time. Similarly, for station 6, a total of 1700 volume scans were collected in the evening from 17:42 to 18:56 local time.

Station 5 had an average of 2259 particle counts across the span of the sampling period; its largest count of 2482 particles followed its smallest count of 2078 particles consecutively. There is a drop in particle counts from the start time until 5:40 and then a plateau until the jump to around 6:20. The counts for station 5 showed more variation than station 6. Station 6 is relatively consistent for the first half hour of sampling. Overall, station 6 showed a higher average particle count of 2347, and showed less variance during the entire sampling period. The highest particle count was 2542 at time 17:47 and the lowest was the last sample at 18:46.

Starting at 18:21 there is a steady decline until the end of the sampling period. This steady decline may represent the falling end of a migration period, but without a longer sampling period it is difficult to make any conclusive argument. A prolonged sampling period at which a full migration cycle is evident would be ideal; for this case, we would expect to see a large flux in particle counts during the migration period and then a drop back to normal level.

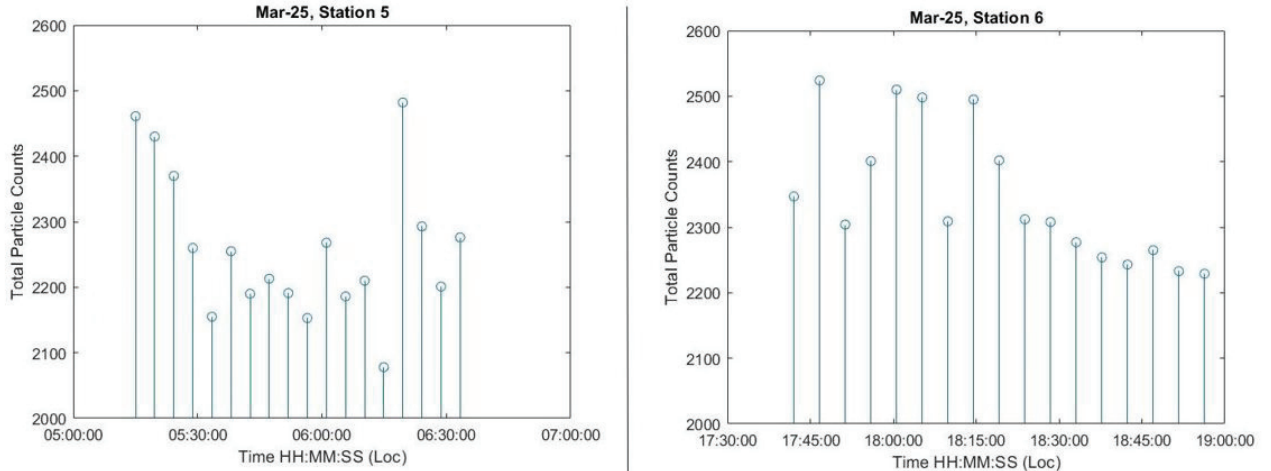


Figure 5.2: Particle counts from stations 5 and 6.

Ideally, during the deployment of the imaging system, we hoped to collect images of schools of fish and krill. The instruments deployed did not capture these large congregations as hoped. The ship EK-80 did record a migration mass moving through the water column during the evening period of station 6, as shown in the acoustic time lapse in figure 5.3

In figure 5.3, the time lapse recorded from 17:00 to 21:00 hours shows a mass moving through the water column as marked in green, this is in coherence with the time series recording for the lidar imager at station 6. The profiler was positioned in the middle of the mass congregation to give the best opportunity of observing the migration. The mass consistently fluctuated between 200 and 300 meters across the same period shown in figure 5.2 for station 6. The acoustic data supports the recorded consistency in particle counts, but analysis of the images themselves and PSDs show a lack of large congregation. This could imply that large schools avoided the profiler, though the lidar itself does not emit a visible beam to marine life. Other instruments include blinking lights and the frame itself is an obstacle, and may have contributed to marine life avoidance.

The priority of the processing method for the UMSLI system is to consistently ex-

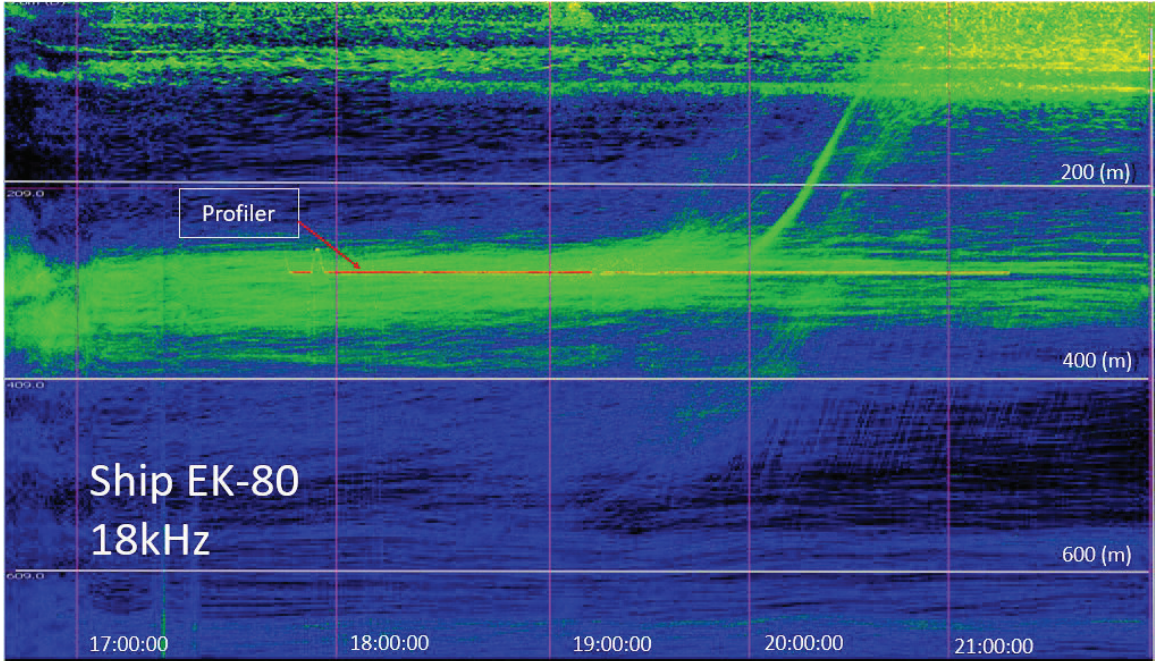


Figure 5.3: EK-80 acoustic time series.

tract significant particles while eliminating the counting of noise and small scattering returns. During experimentation of alternative processing methods, particle counts were conducted that did not include the step of excluding single pixels as extracted particles. This raised particle counts for both stations, the maximum particle count for station 5 reached up to 8000. After further evaluation of the processed image, it was concluded that a single pixel is unlikely a POI and should not be included for evaluation. Further evidence that led to the exclusion of single pixel particles was found in the PSDs as well.

It was found that for particle size bins that equated to the slice resolution of a single pixel showed a very large increase that served as an outlier to the normal PSD trends. Though elimination of single pixel particles also increases the smallest resolvable objects for the system, the particle counts are more reliable with their exclusion. Confidence in this processing approach is also affirmed with the consistency in the particle counts across two different locations.

5.3 PARTICLE SIZE DISTRIBUTIONS

Here we present the distribution and abundance of POI counts across a time series of scans. In order to show the sizing distribution for each sample, we use a particle size distribution (PSD) plot. This method best represents particle abundance for resolvable size resolutions for the UMSLI system. For most cases of underwater optics, PSDs are used to measure much smaller particles, the Sequoia LISST-100X instrument, for example, uses the refraction properties of an intersecting particle through two collimated beams to measure the approximate size of a particulate on the scale of micro-liters per liter [45, 51, 52]. We note here that the path length of the beam in this case is constant, as well the volume observed is unchanged over time. More common optical devices used to generate PSDs that function similarly to the LISST-100X include the Coulter Counter and Flowcam [52, 53]. For the imaging lidar, we observe POI across a dynamic volume and present a sizing distribution on a scale of 2 *cm* to 50 *cm* per 650 *m*³. We observe in the case of imaging lidar, a larger observable volume that expands in space and range of expanding size. Here we aim to express the full spectrum of observable sizes for the UMSLI system and shift the focus to the processing methods ability to accurately size distinguished POI. To do this, we make the assumption that extracted POI are spheres with an equivalent spherical diameter, D , which is measured as $\sqrt{4A/\pi}$ where A is the extracted filled area as demonstrated in the method section [51, 54]. Note that A is a measure of the image pixel count for a POI and the calculated diameter is scaled in accordance to the sizing correction. Thus, the resolution for the discrete sizing bins of the PSDs are presented in accordance to the minimal change in equivalent spherical diameter between two slices. We present the PSDs on a log scale, modeled as a power law or Junge distribution which is mathematically represented below,

$$n(D) = n_o(D/D_o)^{-\gamma} \tag{5.1}$$

where, D_o is the reference diameter, n_o is the differential particle concentration at $D_o(m^{-3}.cm^{-1})$ and $-\gamma$ is the slope of the distribution [37, 51, 54–56].

Most studies when considering PSDs take great interest in the slope, γ , of the distribution, as it indicates to the dominance of smaller or larger particles. We expect to see a larger slope for smaller particle dominance and a smaller slope for larger particles. Typical slopes for small marine particles has a range of -3.5 to -4 with variability depending on the size class [37, 51, 55]. Other expected variations in the slope are caused by high concentrations of bioactivity, seasonal variation and varying size ranges such is the case for the lidar imager [5, 39]. The analysis for the PSDs generated from the imaging lidar does not give high enough particle counts to confidently make any conclusions about the quantitative slope of the distribution, but does allow insight to general trends.

From the PSDs we observe the largest abundance and stability in slope are observed only in the first few size classes. We expect these to be mostly large aggregations of marine snow that are ever present in the water column as they present a stable slope. This is the size class that would typically show a larger fluctuation if noise is present. Stability is an indicator that noise that usually causes image speckle is removed and not analyzed as a POI. More noticeable clumping and variation in the size classes from 5 cm to 10 cm depict the beginning of organisms with transport capability. The slope for this section of data still shows a defined negative slope, slightly smaller than that of smaller size classes. Resolved POI beyond 10 cm are only counted on rare occasions and often form a row on the bottom of the plot. These are expected to be smaller marine organisms such as fish that we expect to be present due to the vertical migration during the morning and evening periods.

The PSDs presented in figure 5.4 are generated from 100 consecutive volumetric scans as they represent the particles in the water columns over a 5 minute period for stations 5 and 6. The presented PSDs are only a few of the 17 samples taken for each

station. The sample chosen for this figure serves to demonstrate similarities as well differences in the PSDs.

One of the immediate concerns with the PSDs are outlier points that do not follow the general slope. For example, in the presented PSDs for station 6, there is a consistent point at 6.8 *cm* that is considerably lower than its neighboring size classes. Though this size class has a very low concentration and could be a error caused by sample size, its consistency is a concern. This could be caused by size gap between the lidar slices. Between each lidar slice in the volume, there is a discrete resolution change of 0.22 *cm*. The breaking up of the scanned volume into discrete slices leads to discontinuity in sizing due to assumptions that a volume slice shares a discrete resolution. This is a limitation of the PMT impulse response and not the digitizer for most lidar systems. Station 6 also shows more cases of larger POI, the largest particle recorded was up to 38.07 *cm*. In general, we find that station 6 recorded larger POI while still showed similar abundance in smaller size classes. The reader may also recall that for many larger POI, we witness a halo effect around the object caused by large reflections. This leads to an over approximation during the calculation of the particle size. Also, select images show long objects that do not fit the approximation as a sphere and in PSDs represent much larger particles. Figure 5.5 accumulates all 1700 volumetric scans for both stations and superimposes the cumulative PSD data together for comparison. When comparing the two stations we observe very similar patterns in the small size classes where there is a significant sample size. Also, we see a reflection of gaps in size class as mentioned above, which is equally apparent for both stations. Station 6 cumulatively recorded larger POI in more abundance, but station 5 and 6 are similar data set in the 10 to 15 *cm* size classes.

Station 5 shows more linearity in the slope in the mid-range size classes, though there are signs of grouping for size classes of 8-9 *cm*. Grouping is caused by the logarithmic scales, but it may also suggest a larger population of POI in this size

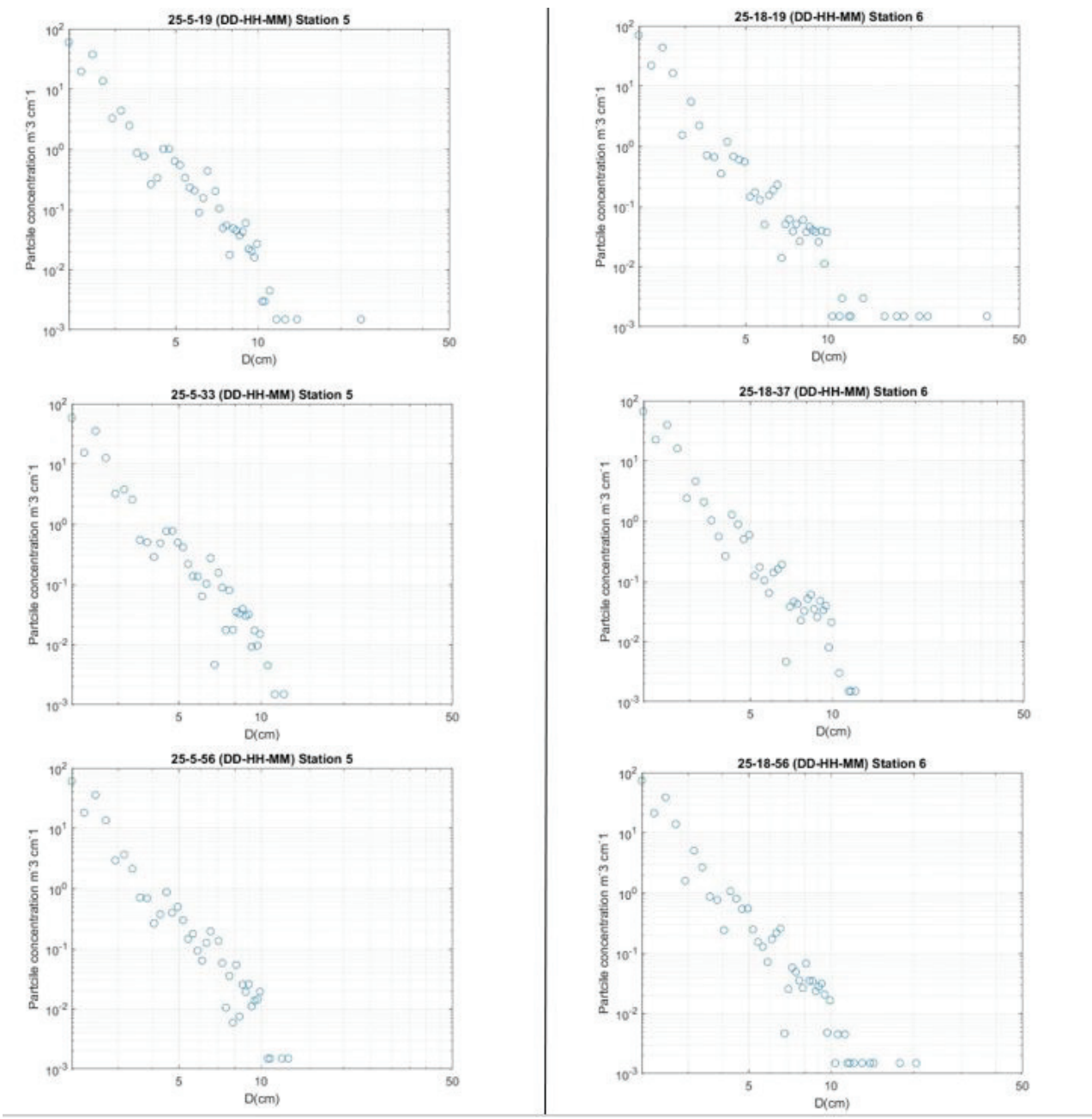


Figure 5.4: Select PSDs from stations 5 and 6.

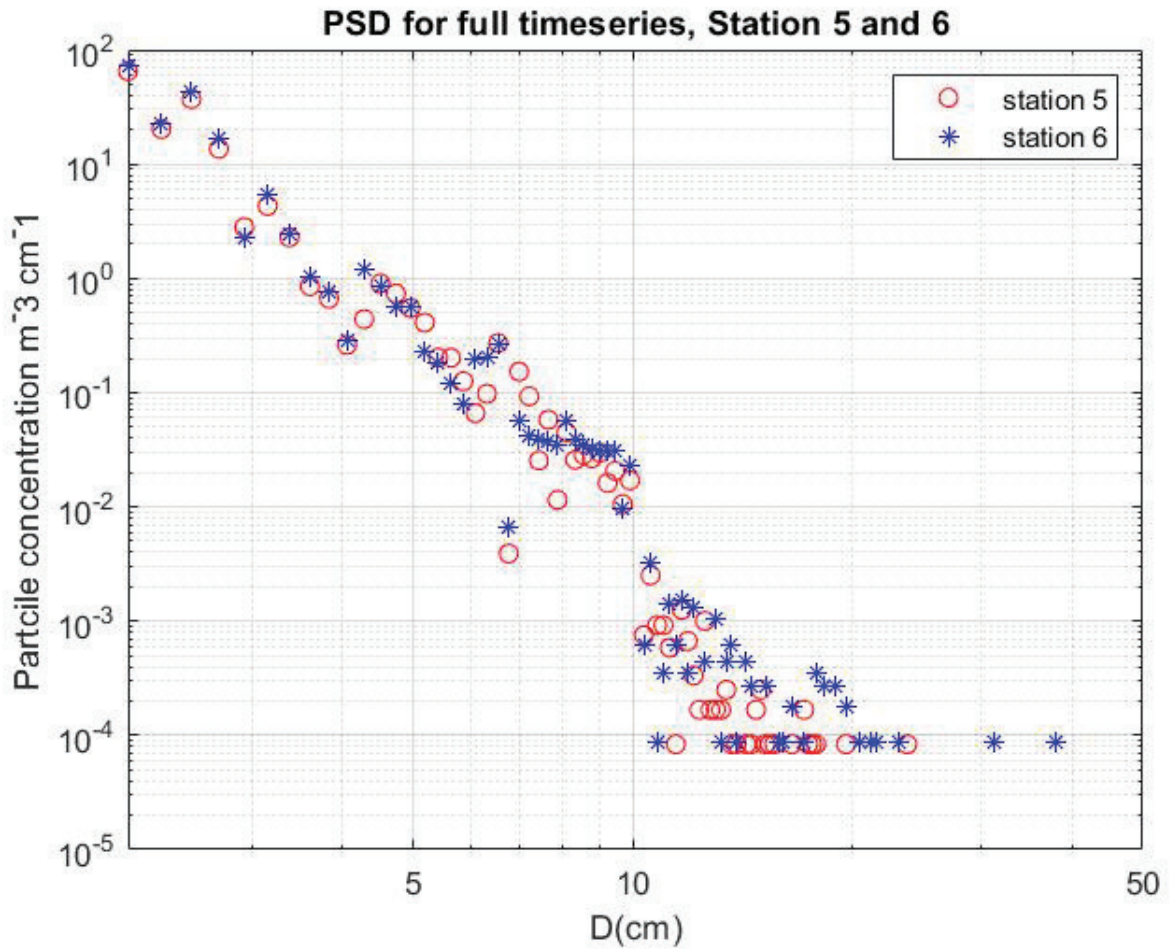


Figure 5.5: Cumulative PSDs from stations 5 and 6.

range. Studies suggest that flat sections in PSDs are indicators of an abundance in organisms of a certain size class and is a sign of bio-activity [37,51]. Again, the sample size for this data set does not allow for any conclusive statement to this regard, though the flux of larger particles at station 5 is evidence that this deployment captured more activity in the water column. In general, the consistency seen in the smaller class size supports consistency using the method for POI extraction, while there is still larger possibility for error caused by assumptions that gives rise to fluctuation in slope. Larger POI are very few, as is expected when observing open ocean waters, though the expectation for larger migrations of fish and krill was not met.

Typically, large sample numbers are easy to accumulate when considering particles on a micrometer scale, as they naturally occur in greater abundance [4]. When conducting particle statistics on objects in the centimeter range, there is a drastic drop of observation per unit volume of water. The UMSLI system does provide an insightful look into PSD for larger particles. The large sample volumes creates opportunity to observe larger particles, while its dynamic resolution extends across a broad size class.

Imaging lidar follows the same principle of measuring scattering to approximate the particle size as many PSD generating instruments. Here, to accommodate the large viewing field, we assume that particle size is a function of not only scattering but its distance from the receiver, as governed by the beam diameter. As previously mentioned, a particle smaller than the beam diameter with a high reflectivity can cause a large response in the recorded waveform that insinuates a larger particle. This is further exaggerated if this occurs in a later volume slice, for which its size is scaled proportionally.

The threshold step in the processing methods is the last time a particle is evaluated in terms of its irradiance intensity. This information is still obtained for every extracted particle, as it could serve to better characterize specific POI, but for this study was not fully utilized statistically. Characterization about the particles composition and shape could be made in relation to its intensity, however, this would require a modeling effort that is specific to this lidar system and experimentation with a larger sampling population of known particulates. Typical particle counter instruments use embedded fixed boundary conditions in the control volume such as, particle size and sampling limit. Here, we extend the capability of a simple elastic lidar to observe an area in the ocean that we largely do not understand, and thus need to engineer a system that is capable of imaging a large range of marine organisms.

CHAPTER 6

CONCLUSION

When considering the performance of the UMSLI system in creating PSDs, we must recognize several disadvantages that are largely due to the system design. The UMSLI system's original design purpose is to survey a large volume for large marine species in the size range of meters. As highlighted in the Development of UMSLI section, the system is capable of resolving images with enough clarity to identify a barracuda or grouper from several meters away. The intentions of the imagers deployment on the cruise to the mesopelagic was to image schools of fish and krill to further demonstrate its imaging capability and provide an overlapping ranging capability between the other optical and acoustic devices. The expected observation of these schools of fish were not met as planned, but the system did provide insight to larger particle distributions. The effort to develop a protocol for evaluation of these observe particles was conducted to exemplify the capabilities of lidar imaging to the limit of its hardware components. The UMSLI system has now opened the door to explore the observation of a particle size class that is largely understudied, and generate PSDs for a much larger observation volume. The imaging system exemplifies its potential for future deployments in the mesopelagic that would provide statistical evidence to validate image processing methods, and extend opportunity to capture images of larger species.

In regard to the construction of PSDs from the lidar images, the number of particles for the captured size class would require a longer sampling duration to accumulate enough particles to validate a distribution model. This system, as a PSD generating instrument, adds many dynamic factors to the PSD processing stage that are

otherwise, consistent in common devices that generate PSDs. For example, devices such as the LISST-100X calculates its particle concentrations over a control volume of one liter, while in the case of the lidar, we observe a much larger volume that is expansive in time. Also, we observe a much larger dynamic size class with the UMSLI system. The focus of most PSDs are in the size range of 1-100 micrometers, which naturally carries a larger abundance of particles in a smaller volume. The abundance of particles in the range of centimeters is not usually considered in the realm of creating PSDs [3, 53, 57]. The path length of the beam for these types of instruments are generally very short in order to avoid beam expansion. For most particle counting devices, the exact size of a particle is based on refractive index, shape, size, and composition. [37, 45, 53, 56].

Before future deployments, technical changes are suggested. The understanding of the rate of beam spreading plays a direct role in the sizing of particles. Extensive study of the point spread function and distortion behavior for highly collimated beams has been conducted in the past, and experimentation to validate a modeling effort of the beam spread for this system would greatly eliminate systematic error [14]. Air and bench top characterization would provide the PMT noise scale factor and give validation of the expected noise scale. Experimentation with differentiating target size and reflection would give baseline estimates for threshold levels and expected noise amplification. Similarly, this same test could be conducted with uniformly sized particle beads at a close range. Just as this experiment can be geared to larger or smaller targets with varying size classes, so can the protocol for POI extraction.

When considering the distribution of POI extracted among image slices, we find the highest abundance of POI counted were in the first 10 evaluated slices. This is expected because of the exponential loss of signal due to attenuation. However, this also often causes saturation in the PMT, ringing, halo effects, and limits accountable information from the waveform. To mitigate this effect, the system could feature a

range gating capability.

Range gating would greatly eliminate unwanted scattering to the system, and give the user control over which size classes are of interest with greater contrast. However, range gating adds complexity and cost to a system, and would in effect create discontinuity between image slices and result in loss of the observable volume. A shorter pulse duration is an optional improvement, as is a PMT with a faster impulse response allows for a faster sampling rate of the system. These upgrades come with extra cost and less reliability. This would be an improvement of the system's imaging ability, but the focus of this study was to extend capability of the imaging system, not improve its hardware and components.

The UMSLI system also features other denser FOVs that were not analyzed with the processing method outlined. The same processing steps could be applied to the denser viewing modes with little changes to the original code and hold potential to resolve smaller particle size classes. The geometry of the beam overlap may allow for multiple points of inflection and more detail on smaller object as demonstrated in figure 1.5. This data is largely un-evaluated and is an extended study of this project. Other un-addressed problems are the jitter effect caused during the scanning process that degrades the original 200 x 200 image into a 200 x 100 image, and calibration to mitigate blurring on the edges of images. These issues are further evaluated and considered with the continued development of lidar imaging systems at HBOI.

BIBLIOGRAPHY

- [1] F. Caimi and F. Dalglish, “Subsea laser scanning and imaging systems,” in *Subsea Optics and Imaging*. Elsevier, 2013, pp. 327–352. [Online]. Available: <https://linkinghub.elsevier.com/retrieve/pii/B9780857093417500133>
- [2] U. Passow and A. L. Alldredge, “Aggregation of a diatom bloom in a mesocosm: The role of transparent exopolymer particles (TEP),” *Deep Sea Research Part II: Topical Studies in Oceanography*, vol. 42, no. 1, pp. 99–109, Jan. 1995. [Online]. Available: <https://linkinghub.elsevier.com/retrieve/pii/096706459500006C>
- [3] J. Taucher, P. Stange, M. Algueró-Muñiz, L. T. Bach, A. Nauendorf, R. Kolzenburg, J. Büdenbender, and U. Riebesell, “In situ camera observations reveal major role of zooplankton in modulating marine snow formation during an upwelling-induced plankton bloom,” *Progress in Oceanography*, vol. 164, pp. 75–88, May 2018. [Online]. Available: <https://linkinghub.elsevier.com/retrieve/pii/S0079661117302240>
- [4] A. K. Vuorenkoski, F. R. Dalglish, M. S. Twardowski, B. Ouyang, and C. C. Trees, “Semi-empirical inversion technique for retrieval of quantitative attenuation profiles with underwater scanning lidar systems,” W. W. Hou and R. A. Arnone, Eds., Baltimore, Maryland, United States, May 2015, p. 94590E. [Online]. Available: <http://proceedings.spiedigitallibrary.org/proceeding.aspx?doi=10.1117/12.2180158>
- [5] L. Stemmann, G. A. Jackson, and D. Ianson, “A vertical model of particle size distributions and fluxes in the midwater column that includes biological and physical processes—Part I: model formulation,” *Deep Sea Research Part I: Oceanographic Research Papers*, vol. 51, no. 7, pp. 865–884, Jul. 2004. [Online]. Available: <https://linkinghub.elsevier.com/retrieve/pii/S0967063704000433>
- [6] J. Jaffe, K. Moore, J. McLean, and M. Strand, “Underwater Optical Imaging: Status and Prospects,” *Oceanography*, vol. 14, no. 3, pp. 64–75, 2001. [Online]. Available: <https://tos.org/oceanography/article/underwater-optical-imaging-status-and-prospects>
- [7] J. S. Jaffe, “Underwater Optical Imaging: The Past, the Present, and the Prospects,” *IEEE Journal of Oceanic Engineering*, vol. 40, no. 3, pp. 683–700, Jul. 2015. [Online]. Available: <http://ieeexplore.ieee.org/document/6930829/>
- [8] F. Dalglish, Bing Ouyang, A. Vuorenkoski, B. Metzger, B. Ramos, and W. Britton, “Extended range distributed laser serial imaging in turbid estuarine

- and coastal conditions,” in *2012 Oceans*. Hampton Roads, VA: IEEE, Oct. 2012, pp. 1–7. [Online]. Available: <http://ieeexplore.ieee.org/document/6405056/>
- [9] F. R. Dalglish, A. K. Vuorenkoski, and B. Ouyang, “Extended-Range Undersea Laser Imaging: Current Research Status and a Glimpse at Future Technologies,” *Marine Technology Society Journal*, vol. 47, no. 5, pp. 128–147, Sep. 2013. [Online]. Available: <http://openurl.ingenta.com/content/xref?genre=article&issn=0025-3324&volume=47&issue=5&spage=128>
- [10] H. M. Zorn, J. H. Churnside, and C. W. Oliver, “LASER SAFETY THRESHOLDS FOR CETACEANS AND PINNIPEDS,” *Marine Mammal Science*, vol. 16, no. 1, pp. 186–200, Jan. 2000. [Online]. Available: <http://doi.wiley.com/10.1111/j.1748-7692.2000.tb00912.x>
- [11] J. Principe, F. R. Dalglish, B. Ouyang, A. K. Vuorenkoski, B. Ramos, Y. Li, and Z. Cao, “MEMS-based serial LiDAR detection and imaging architecture for automated surveillance of undersea marine life,” in *Unconventional Optical Imaging*, C. Fournier, M. P. Georges, and G. Popescu, Eds. Strasbourg, France: SPIE, May 2018, p. 78. [Online]. Available: <https://www.spiedigitallibrary.org/conference-proceedings-of-spie/10677/2309997/MEMS-based-serial-LiDAR-detection-and-imaging-architecture-for-automated/10.1117/12.2309997.full>
- [12] Z. Cao, J. C. Principe, B. Ouyang, F. Dalglish, A. Vuorenkoski, B. Ramos, and G. Alsenas, “Marine animal classification using UMSLI in HBOI optical test facility,” *Multimedia Tools and Applications*, vol. 76, no. 21, pp. 23 117–23 138, Nov. 2017. [Online]. Available: <http://link.springer.com/10.1007/s11042-017-4833-4>
- [13] F. Dalglish, B. Ouyang, A. Vuorenkoski, B. Ramos, G. Alsenas, B. Metzger, Z. Cao, and J. Principe, “Undersea LiDAR imager for unobtrusive and eye safe marine wildlife detection and classification,” in *OCEANS 2017 - Aberdeen*. Aberdeen, United Kingdom: IEEE, Jun. 2017, pp. 1–5. [Online]. Available: <http://ieeexplore.ieee.org/document/8085029/>
- [14] B. M. Cochenour, L. J. Mullen, and A. E. Laux, “Characterization of the Beam-Spread Function for Underwater Wireless Optical Communications Links,” *IEEE Journal of Oceanic Engineering*, vol. 33, no. 4, pp. 513–521, Oct. 2008. [Online]. Available: <http://ieeexplore.ieee.org/document/4769674/>
- [15] F. R. Dalglish, J. J. Shirron, D. Rashkin, T. E. Giddings, A. K. Vuorenkoski Dalglish, I. Cardei, B. Ouyang, F. M. Caimi, and M. Cardei, “Physical layer simulator for undersea free-space laser communications,” *Optical Engineering*, vol. 53, no. 5, p. 051410, Apr. 2014. [Online]. Available: <http://opticalengineering.spiedigitallibrary.org/article.aspx?doi=10.1117/1.OE.53.5.051410>

- [16] M. S. Twardowski, F. R. Dalgleish, A. Tonizzo, A. K. Vuorenkoski Dalgleish, and C. Strait, "Development and assessment of lidar modeling to retrieve IOPs," in *Ocean Sensing and Monitoring X*, W. W. Hou and R. A. Arnone, Eds. Orlando, United States: SPIE, May 2018, p. 32. [Online]. Available: <https://www.spiedigitallibrary.org/conference-proceedings-of-spie/10631/2309998/Development-and-assessment-of-lidar-modeling-to-retrieve-IOPs/10.1117/12.2309998.full>
- [17] L. De Dominicis, "Underwater 3d vision, ranging and range gating," in *Subsea Optics and Imaging*. Elsevier, 2013, pp. 379–410e. [Online]. Available: <https://linkinghub.elsevier.com/retrieve/pii/B9780857093417500157>
- [18] T. E. Giddings, "Numerical simulation of the incoherent electro-optical imaging process in plane-stratified media," *Optical Engineering*, vol. 48, no. 12, p. 126001, Dec. 2009. [Online]. Available: <http://opticalengineering.spiedigitallibrary.org/article.aspx?doi=10.1117/1.3274936>
- [19] L. Mullen, A. Laux, and B. Cochenour, "Propagation of modulated light in water: implications for imaging and communications systems," *Applied Optics*, vol. 48, no. 14, p. 2607, May 2009. [Online]. Available: <https://www.osapublishing.org/abstract.cfm?URI=ao-48-14-2607>
- [20] L. E. Mertens and F. S. Replogle, "Use of point spread and beam spread functions for analysis of imaging systems in water," *Journal of the Optical Society of America*, vol. 67, no. 8, p. 1105, Aug. 1977. [Online]. Available: <https://www.osapublishing.org/abstract.cfm?URI=josa-67-8-1105>
- [21] F. R. Dalgleish, F. M. Caimi, A. K. Vuorenkoski, W. B. Britton, B. Ramos, T. E. Giddings, J. J. Shirron, and C. H. Mazel, "Efficient laser pulse dispersion codes for turbid undersea imaging and communications applications," W. W. Hou and R. A. Arnone, Eds., Orlando, Florida, Apr. 2010, p. 76780I. [Online]. Available: <http://proceedings.spiedigitallibrary.org/proceeding.aspx?doi=10.1117/12.854775>
- [22] D. Matthew, "NASA Goddard Space Flight Center," p. 40.
- [23] F. R. Dalgleish, A. K. Vuorenkoski, G. Nootz, B. Ouyang, and F. M. Caimi, "Experimental imaging performance evaluation for alternate configurations of undersea pulsed laser serial imagers," W. W. Hou and R. Arnone, Eds., Orlando, Florida, United States, May 2011, p. 80300B. [Online]. Available: <http://proceedings.spiedigitallibrary.org/proceeding.aspx?doi=10.1117/12.888640>
- [24] F. Dalgleish, F. Caimi, Y. Wan, W. Britton, J. J. Shirron, T. E. Giddings, C. H. Mazel, J. M. Glynn, and J. P. Towle, "Experimental Validation of a Laser Pulse Time-History Model," p. 8, 2010.

- [25] G. R. Fournier, "Range-gated underwater laser imaging system," *Optical Engineering*, vol. 32, no. 9, p. 2185, 1993. [Online]. Available: <http://opticalengineering.spiedigitallibrary.org/article.aspx?doi=10.1117/12.143954>
- [26] R. Measures, *Laser Remote Sensing fundamentals and applications*. John Wiley & Sons.
- [27] T. Giddings, J. Shirron, and A. Tirat-Gefen, "EODES-3: An Electro-Optic Imaging and Performance Prediction Model," in *Proceedings of OCEANS 2005 MTS/IEEE*. Washington, DC, USA: IEEE, 2005, pp. 1–8. [Online]. Available: <http://ieeexplore.ieee.org/document/1639947/>
- [28] F. R. Dalgleish, F. M. Caimi, W. B. Britton, and C. F. Andren, "Improved LLS imaging performance in scattering-dominant waters," W. W. Hou, Ed., Orlando, Florida, USA, May 2009, p. 73170E. [Online]. Available: <http://proceedings.spiedigitallibrary.org/proceeding.aspx?doi=10.1117/12.820836>
- [29] F. M. Caimi and F. R. Dalgleish, "Performance considerations for continuous-wave and pulsed laser line scan (LLS) imaging systems," *Journal of the European Optical Society: Rapid Publications*, vol. 5, p. 10020s, Apr. 2010. [Online]. Available: https://www.jeos.org/index.php/jeos_rp/article/view/10020s
- [30] B. Ouyang, F. R. Dalgleish, F. M. Caimi, A. K. Vuorenkoski, T. E. Giddings, and J. J. Shirron, "Image enhancement for underwater pulsed laser line scan imaging system," W. W. Hou and R. Arnone, Eds., Baltimore, Maryland, USA, Jun. 2012, p. 83720R. [Online]. Available: <http://proceedings.spiedigitallibrary.org/proceeding.aspx?doi=10.1117/12.920710>
- [31] F. Dalgleish, B. Ouyang, and A. Vuorenkoski, "A unified framework for image performance enhancement of extended range laser seabed survey sensors," in *2013 IEEE International Underwater Technology Symposium (UT)*. Tokyo: IEEE, Mar. 2013, pp. 1–7. [Online]. Available: <http://ieeexplore.ieee.org/document/6519906/>
- [32] "MEMS Mirrors." [Online]. Available: <https://www.mirrorcletech.com/wp/products/mems-mirrors/>
- [33] B. Ouyang, F. R. Dalgleish, F. M. Caimi, T. E. Giddings, J. J. Shirron, A. K. Vuorenkoski, W. Britton, B. Metzger, B. Ramos, and G. Nootz, "Compressive sensing underwater laser serial imaging system," *Journal of Electronic Imaging*, vol. 22, no. 2, p. 021010, Mar. 2013. [Online]. Available: <http://electronicimaging.spiedigitallibrary.org/article.aspx?doi=10.1117/1.JEI.22.2.021010>
- [34] M. Massot-Campos and G. Oliver-Codina, "Optical Sensors and Methods for Underwater 3d Reconstruction," *Sensors*, vol. 15, no. 12, pp. 31 525–31 557, Dec. 2015. [Online]. Available: <http://www.mdpi.com/1424-8220/15/12/29864>

- [35] J. Schulz, “Geometric optics and strategies for subsea imaging,” in *Subsea Optics and Imaging*. Elsevier, 2013, pp. 243–276e. [Online]. Available: <https://linkinghub.elsevier.com/retrieve/pii/B9780857093417500108>
- [36] P. Mariani, I. Quinoces, K. Haugholt, Y. Chardard, A. Visser, C. Yates, G. Piccinno, G. Reali, P. Risholm, and J. Thielemann, “Range-Gated Imaging System for Underwater Monitoring in Ocean Environment,” *Sustainability*, vol. 11, no. 1, p. 162, Dec. 2018. [Online]. Available: <http://www.mdpi.com/2071-1050/11/1/162>
- [37] M. S. Twardowski, E. Boss, J. B. Macdonald, W. S. Pegau, A. H. Barnard, and J. R. V. Zaneveld, “A model for estimating bulk refractive index from the optical backscattering ratio and the implications for understanding particle composition in case I and case II waters,” *Journal of Geophysical Research: Oceans*, vol. 106, no. C7, pp. 14 129–14 142, Jul. 2001. [Online]. Available: <http://doi.wiley.com/10.1029/2000JC000404>
- [38] “R11265u SERIES / H11934 SERIES.” [Online]. Available: <http://dtsheet.com/doc/1279384/r11265u-series---h11934-series>
- [39] A. B. Burd and G. A. Jackson, “Particle Aggregation,” *Annual Review of Marine Science*, vol. 1, no. 1, pp. 65–90, Jan. 2009. [Online]. Available: <http://www.annualreviews.org/doi/10.1146/annurev.marine.010908.163904>
- [40] Z. Liu, W. Hunt, M. Vaughan, C. Hostetler, M. McGill, K. Powell, D. Winker, and Y. Hu, “Estimating random errors due to shot noise in backscatter lidar observations,” *Applied Optics*, vol. 45, no. 18, p. 4437, Jun. 2006. [Online]. Available: <https://www.osapublishing.org/abstract.cfm?URI=ao-45-18-4437>
- [41] P. R. Prucnal and B. E. A. Saleh, “Transformation of image-signal-dependent noise into image-signal-independent noise,” *Optics Letters*, vol. 6, no. 7, p. 316, Jul. 1981. [Online]. Available: <https://www.osapublishing.org/abstract.cfm?URI=ol-6-7-316>
- [42] S. W. Hasinoff, “Photon, Poisson Noise,” in *Computer Vision*, K. Ikeuchi, Ed. Boston, MA: Springer US, 2014, pp. 608–610. [Online]. Available: http://link.springer.com/10.1007/978-0-387-31439-6_482
- [43] J. Minkoff, “Shot Noise and Optical Receivers,” in *Signal, Noise, and Active Sensors Radar, Sonar, Laser Radar*. John Wiley and Sons, INC.
- [44] A. Foi, M. Trimeche, V. Katkovnik, and K. Egiazarian, “Practical Poissonian-Gaussian Noise Modeling and Fitting for Single-Image Raw-Data,” *IEEE Transactions on Image Processing*, vol. 17, no. 10, pp. 1737–1754, Oct. 2008. [Online]. Available: <http://ieeexplore.ieee.org/document/4623175/>
- [45] R. A. Reynolds, D. Stramski, V. M. Wright, and S. B. Woźniak, “Measurements and characterization of particle size distributions in coastal waters,” *Journal*

- of Geophysical Research*, vol. 115, no. C8, p. C08024, Aug. 2010. [Online]. Available: <http://doi.wiley.com/10.1029/2009JC005930>
- [46] H.-T. Fang and D.-S. Huang, “Noise reduction in lidar signal based on discrete wavelet transform,” *Optics Communications*, vol. 233, no. 1-3, pp. 67–76, Mar. 2004. [Online]. Available: <https://linkinghub.elsevier.com/retrieve/pii/S0030401804000380>
- [47] B. Choksi, A. Venkitaraman, and S. Mali, “Finding Best Fit for Hand-Drawn Curves using Polynomial Regression,” *International Journal of Computer Applications*, vol. 174, no. 5, pp. 20–23, Sep. 2017. [Online]. Available: <http://www.ijcaonline.org/archives/volume174/number5/choksi-2017-ijca-915390.pdf>
- [48] N. Otsu, “A Threshold Selection Method from Gray-Level Histograms,” *IEEE Transactions on Systems, Man, and Cybernetics*, vol. 9, no. 1, pp. 62–66, Jan. 1979. [Online]. Available: <http://ieeexplore.ieee.org/document/4310076/>
- [49] D. Bradley and G. Roth, “Adaptive Thresholding using the Integral Image,” *Journal of Graphics Tools*, vol. 12, no. 2, pp. 13–21, Jan. 2007. [Online]. Available: <https://www.tandfonline.com/doi/full/10.1080/2151237X.2007.10129236>
- [50] R. Gonzalez, R. Woods, and S. Eddins, *Digital Image Processing using MATLAB*, 2nd ed.
- [51] A. R. Nayak, M. N. McFarland, J. M. Sullivan, and M. S. Twardowski, “Evidence for ubiquitous preferential particle orientation in representative oceanic shear flows: Nonrandom particle orientation in ocean,” *Limnology and Oceanography*, vol. 63, no. 1, pp. 122–143, Jan. 2018. [Online]. Available: <http://doi.wiley.com/10.1002/lno.10618>
- [52] E. Boss, W. Slade, and P. Hill, “Effect of particulate aggregation in aquatic environments on the beam attenuation and its utility as a proxy for particulate mass,” *Optics Express*, vol. 17, no. 11, p. 9408, May 2009. [Online]. Available: <https://www.osapublishing.org/oe/abstract.cfm?uri=oe-17-11-9408>
- [53] M. Jonasz, “Particle-size distributions in the Baltic,” *Tellus B*, vol. 35B, no. 5, pp. 346–358, Nov. 1983. [Online]. Available: <http://www.tellusb.net/index.php/tellusb/article/view/14624>
- [54] E. Boss, M. S. Twardowski, and S. Herring, “Shape of the particulate beam attenuation spectrum and its inversion to obtain the shape of the particulate size distribution,” *Applied Optics*, vol. 40, no. 27, p. 4885, Sep. 2001. [Online]. Available: <https://www.osapublishing.org/abstract.cfm?URI=ao-40-27-4885>
- [55] J. B. Liley, “Fitting Size Distributions to Optical Particle Counter Data,” *Aerosol Science and Technology*, vol. 17, no. 2, pp. 84–92, Jan. 1992. [Online]. Available: <http://www.tandfonline.com/doi/abs/10.1080/02786829208959562>

- [56] J. C. Kitchen, J. R. V. Zaneveldan, and H. Pak, "Effect of particle size distribution and chlorophyll content on beam attenuation spectra," *Applied Optics*, vol. 21, no. 21, p. 3913, Nov. 1982. [Online]. Available: <https://www.osapublishing.org/abstract.cfm?URI=ao-21-21-3913>
- [57] A. Khelifa and P. S. Hill, "Models for effective density and settling velocity of -ocs Models pour la densité effective et la vitesse de sédimentation de -ocs," p. 12.